Estimation of Latent Heating of Rainfall during the Onset of the Indian Monsoon Using TRMM PR and Radiosonde Data

Ramata Magagi and Ana P. Barros

Division of Engineering and Applied Sciences, Harvard University, Cambridge, Massachusetts

ABSTRACT

The objective of this study is to estimate the vertical structure of the latent heating of precipitation in the vicinity of the Himalayas. Based on a cloud physics parameterization and the thermodynamic equilibrium equation, a simple algorithm is proposed to estimate latent heating from a combination of radiosonde and Tropical Rainfall Measuring Mission (TRMM) precipitation radar (PR) data, specifically, the radar reflectivity and the rain-rate estimates. An evaluation of the algorithm against 6-hourly areal averages from diagnostic budget studies during the South China Sea Monsoon Experiment (SCMEX) suggests that the algorithm captures well the vertical structure of latent heating between the top of the moist layer and the cloud-top detrainment layer. The retrieval algorithm was applied systematically over the Indian subcontinent and Tibetan plateau within a region comprising $15°–32°N$ and $70°–95°E$ during June, the month of monsoon onset, for three different years (1999, 2000, and 2001). The estimated latent heating profiles exhibit large spatial and temporal variability in the magnitude and position of maximum latent heating within the same TRMM overpass, and from one year to the next. This reflects the presence of convective activity with varying degrees of organization during the monsoon, and also the interannual variability of large-scale conditions. Along the Himalayan range, the diurnal cycle of latent heating profiles suggests more intense convective activity in the early morning and during nighttime (1-km difference in the height of maximum latent heating), consistent with the diurnal cycle of rainfall observations and cloudiness. The height of maximum latent heating at stations in the Indian subcontinent varies over a wide range, reflecting a mix of stratiform and convective precipitation systems, respectively, 5.7 ± 2, 3.8 ± 1.5, and 4.8 ± 1.7 km MSL, for 1999, 2000, and 2001. Overall, the peak production of latent heating is roughly at the effective terrain elevation of the Himalayan range with regard to synoptic circulation and orographic enhancement effects. The Tibetan plateau behaves as an elevated heat source with maximum heating produced at 7–8 km MSL. Average values of the maximum latent heating ranged between 1.3 and 1.6 K day^{-1} per unit rainfall (1 cm day^{-1}), with maximum values of up to 10 K day^{-1}.

1. Introduction

The motivation for this work is to elucidate the role of the Himalayan range in the transfer of atmospheric moisture between the Tibetan plateau and the Indian subcontinent, and, therefore, the role of the mountains in regional monsoon dynamics as suggested by previous studies (Lang and Barros 2002; Barros at al. 2003). Because of the small spatial gradients of temperature in the Tropics and equatorial regions, the release of latent heat during precipitation is essential in maintaining atmospheric convergence, fueling the vertical motion of convective systems, and large-scale circulations (Krishnamurti and Bhalme 1976; Webster 1983; Lau and Peng 1987, among others).

During the monsoon, heavy rainfall persists over the Indian subcontinent and the Himalayas from the end of

May to the beginning of October. Recently, Lang and Barros (2002) investigated the features of the 1999 and 2000 monsoon onsets in Nepal. They showed that the monsoon onset is mainly driven by depressions in the Bay of Bengal that reach the Himalayas and cause heavy rainfall continuously during two–three periods. Specifically, between 10% and 20% of all monsoon rainfall fell during 12–13 June 1999 and 7–8 June 2000. Because of the high rainfall accumulations along the Himalayas during the monsoon, one interesting research question is to quantify the associated latent heating release and its impact on the regional energy budget of the atmosphere.

Latent heating is released in cloudy regions as a result of condensation processes. The fundamental physics are strong vertical motion that forces moist air parcels upward, and the saturation and condensation of moist air as it reaches colder levels. Because atmospheric latent heating cannot be measured directly, it is usually estimated using models or parameterizations of moist processes in the atmosphere. Some approaches rely on cu-

Corresponding author address: Dr. Ana P. Barros, Division of Engineering and Applied Sciences, Pierce Hall 118, Harvard University, 29 Oxford Street, Cambridge, MA 02138.
E-mail: barros@deas.harvard.edu

mulus ensemble models that require the vertical distribution of hydrometeors in the lower atmosphere as input (Tao et al. 1990; Olson et al. 1999). Others rely on the parameterization of cumulus convection based on the use of the thermodynamic equilibrium equation and the moisture and the heat budget equations (Yanai et al. 1973; Chang 1976; Holton 1979; Stevens et al. 1977; Stevens and Lindzen 1978; Hartman et al. 1984; Houze 1982, 1989).

To assess the role of the Himalayas on the energy budget of the monsoon, we need to be able to analyze the spatial and temporal variability of latent heating regionally in a systematic manner. Previously, a large number of investigations using Tropical Rainfall Measuring Mission (TRMM) data (available online at http://trmm.gsfc.nasa.gov) focused on estimating the vertical and horizontal distributions of tropical rainfall (Adler et al. 2000; Aonashi and Liu 2000; Kummerow et al. 2000; Viltard et al. 2000, etc.). Generally, these studies relied on radar reflectivity–rain rate (Z–R) relationships, or on the combination of the TRMM precipitation radar (PR) and the TRMM Microwave Imager (TMI) data. With regard to the retrieval of latent heating, fewer TRMM-based investigations are found in the literature, especially for continental regions (e.g., Tao et al. 2001). Here, we describe a simple algorithm to estimate the vertical profile of latent heating, modified after a parameterization of deep cumulus convection proposed by Stevens et al. (1977) and Stevens and Lindzen (1978), and the use of the basic equations of thermodynamics. The relevant input data are the vertical profile of the radar reflectivity measured by the TRMM PR, the estimated rain rate at the top of the moist layer, and radiosonde data. Evaporative cooling is estimated following the scheme proposed by Barros and Lettenmaier (1994).

Our strategy to develop a PR-based latent heating retrieval algorithm for continental regions takes place in two phases: 1) radiosonde data are used to estimate parameters not directly obtainable from the TRMM PR 2A25 data (profile estimation algorithm); and 2) diagnostic relationships are developed between algorithm parameters, PR data, and model simulations, which could be used to estimate latent heating profiles where radiosonde stations do not exist (general algorithm). The first step is described in this manuscript; the second step is part of ongoing research.

The results presented here are distributed within the region 15°–32°N, 70°–95°E for June 1999, 2000, and 2001 (see Fig. 2a). Our domain of study is much larger than our region of interest because we need to include a large number of radiosonde stations to proceed to step 2 of algorithm development, having assessed its skill in a statistically meaningful way. The context for the development of the algorithm is discussed in section 2. Section 3 provides a description of the data, data-related implementation issues, and algorithm evaluation against the South China Sea Monsoon Experiment (SCSMEX)

data. Systematic retrieval results are analyzed in section 4, and the paper concludes with comments and discussion in section 5.

2. Algorithm rationale

Previously, many different approaches were developed for estimating latent heating indirectly using various algorithms based on cumulus ensemble models and parameterizations of cumulus convection. For example, Yanai et al. (1973) used observations to derive large-scale heat and moisture budgets, and a simple cumulus model to infer cloud properties (mass flux, moisture, etc.). With satellite data, the challenge is how to relate latent heating to the vertical distribution of hydrometeors and the dynamics of mass exchange among cloud layers (moisture fluxes). Tao et al. (1990) developed a simple algorithm that relates vertical heating profiles to estimates of the corresponding hydrometeor profiles from the Goddard Cumulus Ensemble (GCE) model. Later, to include explicitly the difference in microphysical processes in convective and stratiform rain systems, Tao et al. (1993, hereinafter TAO) used the relative proportion of stratiform and convective rainfall derived from model profiles to constrain the vertical structure of the retrieved latent heating profile.

Cartwright and Ray (1999) relied on reflectivity profiles measured from a ground-based radar to develop a latent heating estimation algorithm. The radar measurements were first used to distinguish convective from stratiform rainfall. Then, a principal component analysis was applied to model-derived (GCE) latent heating to infer the principal modes of variability as a function of rainfall type and reflectivity profile. These were used subsequently along with observed reflectivity profiles to estimate the corresponding latent heating distributions.

Several studies were conducted to retrieve latent heating from the Special Sensor Microwave Imager (SSM/I), including Olson et al. (1999, hereinafter OL), and Yang and Smith (1999, hereinafter YS). The working premise of these algorithms is to find the pair of latent heating and hydrometeor profiles that matches, in some optimal sense, an ensemble of microwave radiometric observations at different frequencies and polarizations. Important differences between the two is that surface rainfall is related to the vertically integrated latent heating in the OL algorithm, while the variation of raindrop mass flux with height is used to generate the latent heating profile in the YS algorithm. Olson et al. (1999) discussed the difficulty of separating convective and stratiform rain areas within the spatial resolution of the SSM/I 85-GHz channel (13 km × 15 km). However, the 85.5-GHz channel of TMI and the TRMM PR sensors provides data at a much higher spatial resolution (5 km × 7 km and 4.3 km × 4.3 km, respectively), and, thus, this problem should be less important. Recently, based on the combined use of cloud models and

TRMM PR and TMI rainfall estimates, Tao et al. (2001) used three different algorithms (i.e., TAO, OL, and YS) to infer the vertical and horizontal distributions of latent heating over oceans and continental regions. They found significant differences between the heating profiles of convective and stratiform rainfall—a single mode profile with peak latent heating in the lower (<600 hPa) troposphere for convective rainfall, a dual-mode profile with significant latent heating release in the upper troposphere ($\cong 300$ hPa), and maximum cooling between 700 and 800 hPa for the case of stratiform rainfall. The ability to separate the two types of heating profiles is important because differences in the vertical structure of latent heating reflect the spatial organization of mesoscale circulations and large-scale dynamics in the Tropics, especially in the case of convective systems, which exhibit large spatial variability (e.g., Lau and Peng 1987; Sui and Lau 1989; Hartmann et al. 1984, among others).

Overall, existing algorithms are based on assumptions regarding the relationships among cloud types, cloud properties, the vertical profile of hydrometeors, and the vertical profile of latent heating in the atmosphere. Because of the lack of in situ measurements, only crude validation through comparison with estimates from radiosondes and with observed hydrometeor distributions and rainfall observations is possible (Houze 1989; Halverson et al. 1996; Yang and Smith 1999; Tao et al. 2001).

Next, we describe the context for the formulation of our algorithm and its implementation.

a. Previous work

In the Tropics, deep cumulus clouds produce most of rainfall and, thus, play an important role in the heat balance of the tropical atmosphere (Chang 1976; Tiedke 1989, among others). The large-scale vertical distribution of the heating can be expressed as follows:

$$LH(z) \approx \sigma_{cloud}(z)Q_{rc}(z) + \underbrace{\sigma_c(z)L_v[c_{cu}(z) - e_{cd}(z)]}_{(ii)}$$

$$+ \underbrace{\sigma_s(z)L_v[c_{su}(z) - e_{sd}(z)]}_{(iii)} - \sigma_s(z)L_f m(z)$$

$$- \frac{\partial}{\partial p}\sum_i \sigma_{i\omega_{vi}(z)}[s_i(z) - s_e(z)], \quad (1)$$

where σ_{cloud}, σ_c, and σ_s are the fractional areal extent of cloud cover, and convective and stratiform precipitation, respectively; Q_{rc} is the net radiative heating in cloud; L_v and L_f are the latent heating of vaporization and fusion, respectively; c_{cu} and c_{su} are the convective and stratiform regions updraft condensation rates, respectively; e_{cd} and e_{sd} are the convective and stratiform regions downdraft evaporation rates, respectively; m is the melting rate in the stratiform region; p is the pressure; ω_v, is the vertical velocity in pressure coordinates, s is the dry static energy; and the subscripts e and i refer, respectively, to the environment and to the various subdivisions of the cloud area (Houze 1982). The dominant terms in Eq. (1) are (ii) and (iii), which represent the net latent heating production from condensation and evaporation processes for convective and stratiform precipitations, respectively. These two terms are proportional to $\omega(z)$, the mean profile of the vertical velocity in Cartesian coordinates. Houze (1989) assumed a one-dimensional weakly entraining jet cumulus model to derive the vertical profile of $\omega(z)$, and the magnitude of ω was scaled according to the amount of convective precipitation. When comparing results for mesoscale convective systems (MCSs) with results from Johnson (1982), including the effects of small cumulus, Houze found that the magnitude of maximum heating was similar, but that the level of the maximum heating was 1 km above that reported by Johnson. This was partly attributed to the weakly entraining jet model, which overestimates the mass flux within the cloud leading to overheating at upper levels (Houze 1989). That is, the challenge in estimating the vertical structure of latent heating is in the determination of the profile of vertical velocity.

Previously, Stevens et al. (1977) developed a parameterization of tropical cumulus convection that accounts explicitly for the vertical transport of horizontal momentum by cumulus clouds, and the vertically integrated heat and moisture budgets. The basic premise of their approach is that all moisture supplied laterally to the clouds via horizontal convergence in the moist layer condenses and contributes to precipitation. The moist layer corresponds to the region of significant moisture convergence near the cloud base (Augustin and Schmidt 1974; Stevens and Lindzen 1978). Neglecting radiative cooling and surface fluxes, the total heating is, therefore, proportional to the surface precipitation. This reflects the balance between latent heating and adiabatic cooling. Precipitation in turn is proportional to the vertical cloud mass flux Mc_{ml} (and vertical velocity ω_{ml}) at the top of the moist layer, the so-called consistency condition. Stevens et al. (1977) and Stevens and Lindzen (1978) specify the functional form of the vertical heating profile LH (z) such that the consistency condition is verified, and the heating function is continuous in the interior of the cloud between cloud base and cloud top:

$$LH(z) = \begin{cases} \alpha[p(z) - p_t][p(z) - p_2][p(z) - p_3] \\ \qquad\qquad p_t \leq p(z) \leq p_{ml} \\ LHS\left[\dfrac{p_b - p(z)}{p_b - p_{ml}}\right]^{\mu} \qquad p_{ml} \leq p(z) \leq p_b \\ 0 \qquad\qquad\qquad \text{elsewhere,} \end{cases} \quad (2)$$

where p_{ml} is the pressure at the top of the moist layer; LHS $= LH(p_{ml})$ is the latent heating at the top of the moist layer; and α, P_2, P_3, and μ are calibration pa-
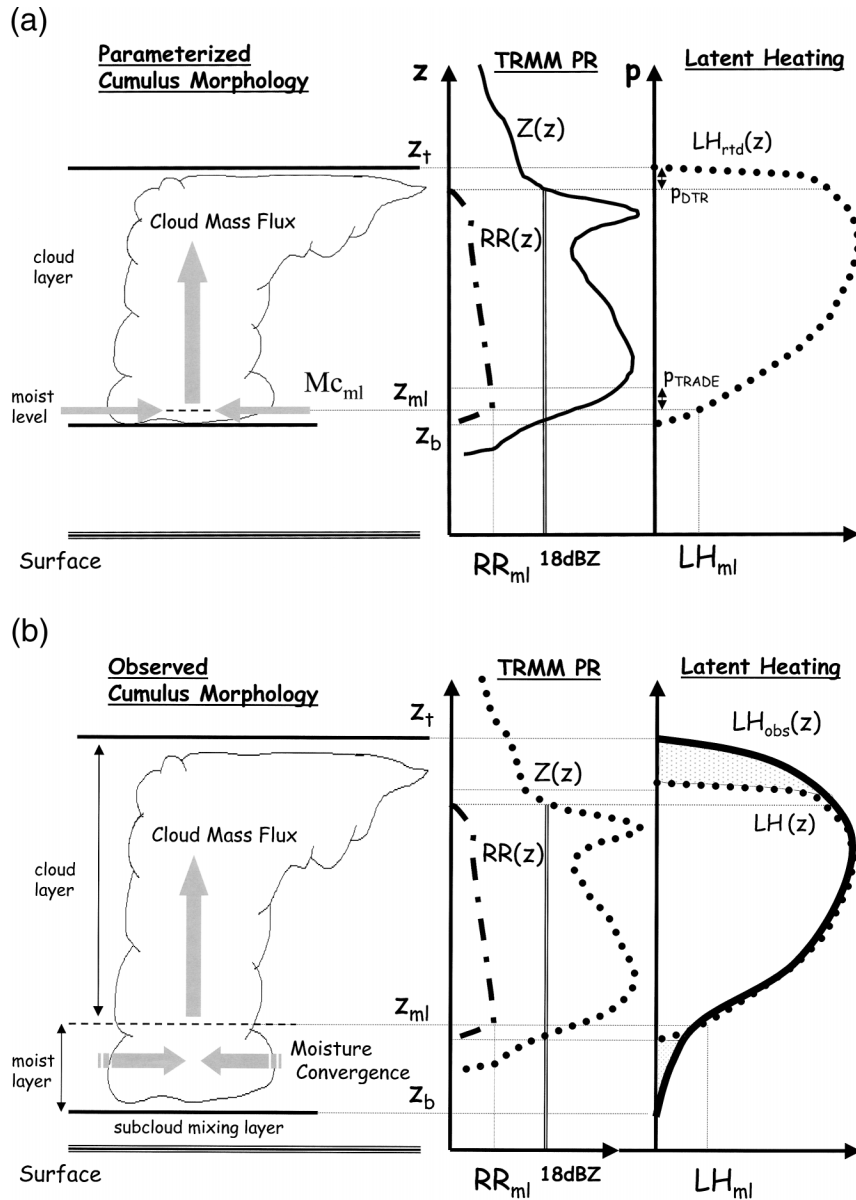
FIG. 1. (a) Parameterization of the vertical morphology of rain-producing clouds in the retrieval algorithm, and (b) comparison between the vertical morphology of rain-producing clouds in the algorithm (retrieved) against that derived from analysis of radiosonde data (observed): z_t − cloud top; z_{ml} − moist level; z_b − cloud base; $LH_{rtd}(z)$ − retrieved latent heating profile; $LH_{obs}(z)$ − observed latent heating profile.

rameters describing the vertical structure of the cloud mass flux $Mc(z)$ as follows:

$$\frac{Mc(z)}{Mc_{ml}} = \left\{ 1 - \exp\left[-\frac{p(z) - p_t}{p_{DTR}}\right]\right\}$$

$$+ \; \varepsilon_c \left\{ \exp\left[-\frac{p_b - p(z)}{p_{TRADE}}\right] - \exp\left(-\frac{p_b - p_t}{p_{TRADE}}\right)\right\},$$

$$(3)$$

where Mc_{ml} is the magnitude of the corresponding deep cloud mass flux (assumed to be proportional to the precipitation); p_t and p_b are the pressures at the cloud top and cloud base, respectively; and p_{DTR} and p_{TRADE} are the depths of the detrainment and trade layers, respectively, at the cloud top (height z_t) and cloud base (height z_b). Between the cloud base and trade level $Mc(z) \gg Mc(z) \Rightarrow Mc_{ml}$ between the trade level and the top of the moist layer, $Mc(z) \approx Mc_{ml}$ above the moist layer, and $Mc(z) \Rightarrow 0$ in the detrainment layer (Figs. 1a and
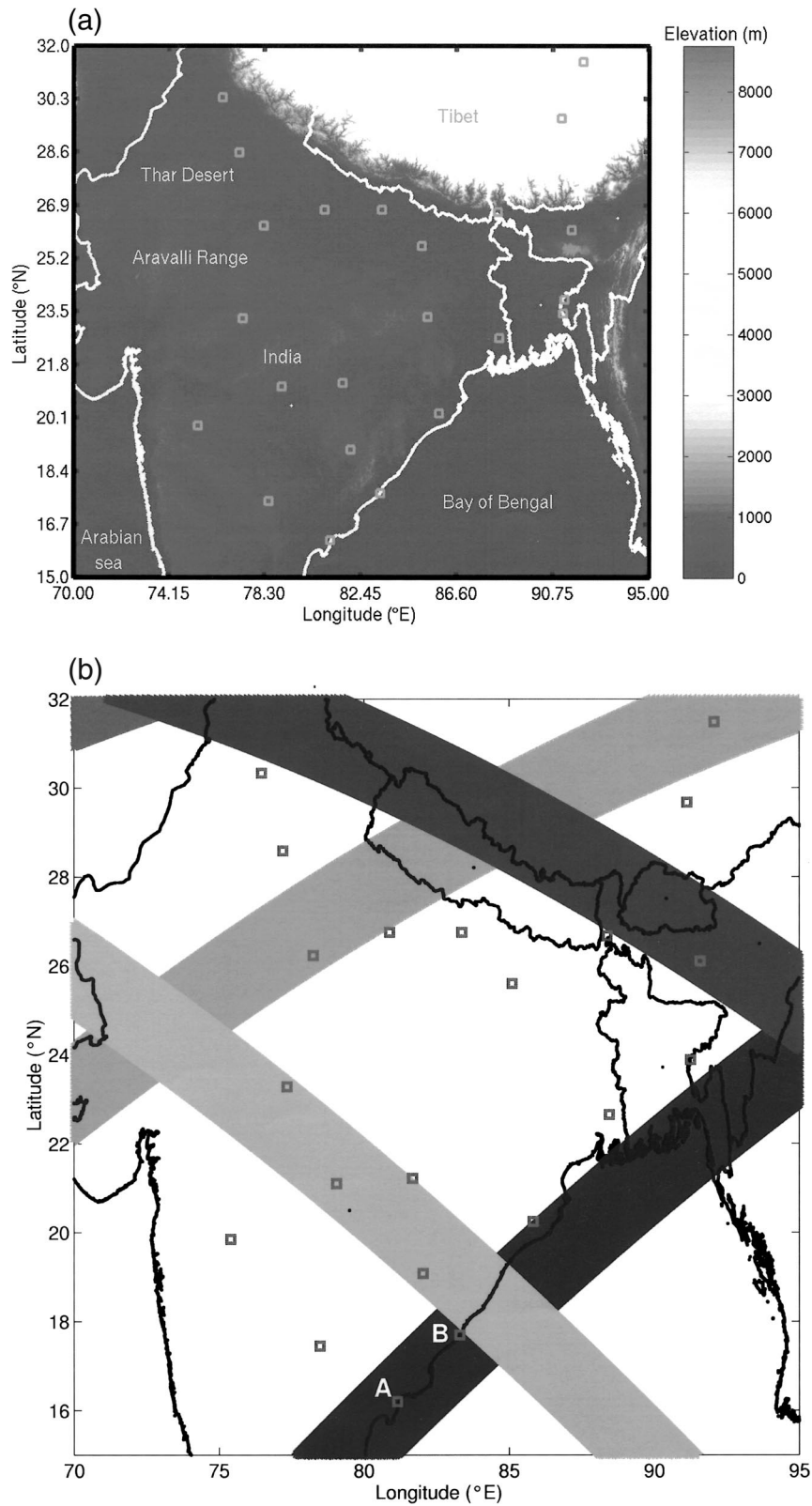
FIG. 2. (a) Spatial coverage of the radiosondes over the study area during Jun 1999. (b) Example of the spatial layout of TRMM PR overpasses and radiosonde locations over the study area on 17 Jun 1999.

TABLE 1. Summary of TRMM PR overpasses, radiosonde data, and latent heating profiles.

| Months | Processed data | | Remaining data after criteria | | Latent heating profiles |
	PR 2A25	Radio-sondes	PR 2A25	Radio-sondes	
Jun 1999	179	136	21	30	1590
Jun 2000	182	70	14	15	475
Jun 2001	180	75	20	22	778

1b). For a standard atmosphere, $\varepsilon_c = 0.5$ and $p_{DTR} = p_{TRADE} = 50$ hPa (Stevens et al. 1977).

Although this parameterization avoids the requirement to determine explicitly the vertical velocity profile, the need to specify the calibration parameters in Eq. (2), as well as cloud parameters in Eq. (3), complicates and restricts its application to the availability of radiosonde data. We propose an alternative approach modified after Stevens et al. (1977) and Stevens and Lindzen (1978), which allows us to extend the applicability of the parameterization by relying on TRMM PR data.

b. Proposed algorithm

Similar to Stevens and Lindzen (1978), neglecting radiation and surface fluxes, and assuming that all condensed water vapor is converted into rain, the integrated heating between the moist level and cloud top is proportional to the integrated cloud mass flux (moisture convergence), and to surface rainfall RR_0 (Yanai et al. 1973):

$$\int_0^\infty \overline{\rho} C_p LH(z) \, dz = L_c \overline{q} \int_{z_b}^{z_t} \frac{\partial Mc(z)}{\partial z} \, dz = L_c RR_0, \quad (4)$$

where L_c is the latent heating of condensation, and the bar symbol is indicative of average values in the well-mixed moist layer. The vertical profile of latent heating can then be expressed as follows:

$$LH(z) = \frac{L_c}{\overline{\rho} C_p} \frac{RR_0}{(z_t - z_b)} \eta(z), \quad (5)$$

where $\eta(z)$ is a dimensionless shape function that behaves similarly to the large-scale mass flux $Mc(z)$ constrained to the consistency condition $[\eta(z_{ml}) = 1]$ as explained below. The expression of $LH(z)$, given by Eq. (5), is close to that found in Holton (1979), with the difference being that the latter corresponds to average tropical conditions and, thus, does not account for the vertical structure of clouds explicitly.

As per Stevens and Lindzen (1978), we assume that all moisture convergence takes place below the top of the moist level (z_{ml}), and, thus, the moisture budget equation can be written as

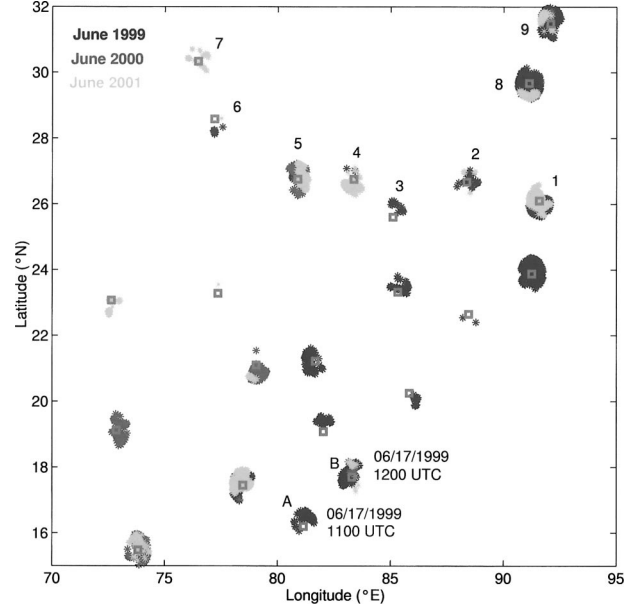$$RR_0 = -\overline{q} \int_0^{z_{ml}} \nabla \cdot (\overline{\rho} v) \, dz. \quad (6)$$

FIG. 3. Areas covered by TRMM PR measurements that satisfied the temporal, horizontal, and vertical criteria with the radiosonde data. The acquisitions are for Jun 1999, Jun 2000, and Jun 2001. The retrievals for the areas marked with characters A, B, and 1–9 are discussed in the paper.

Considering the anelastic form of the mass continuity equation,

$$\nabla \cdot (\overline{\rho} v) + \frac{\partial}{\partial z}(\overline{\rho} \omega) = 0, \quad (7)$$

and combining Eqs. (6) and (7), the surface rain rate RR_0 can be estimated in terms of moisture convergence:

$$RR_0 = \overline{q}_{ml} \int_0^{z_{ml}} \frac{\partial}{\partial z}(\overline{\rho} \omega) \, dz = \overline{q}_{ml} \overline{\rho}_{ml} \omega_{ml}. \quad (8)$$

Following Yanai et al. (1973), if the entire ascent required by the large-scale convergence takes place in the cloud (i.e., the role of convergence is to supply moisture to maintain the heating), then the cloud mass flux can be simply described by

$$Mc(z) = \rho(z)\omega(z). \quad (9)$$

A key step in the proposed parameterization is to express the vertical profile of the moisture flux as a function of the average values of moisture and velocity states in the moist layer (all water vapor that converges horizontally to the moist layer contributes to the cloud mass flux; Figs. 1a,b):

$$\rho(z)\omega(z)q(z) = \overline{q}_{ml} \overline{\rho}_{ml} \omega_{ml} \eta(z), \quad (10)$$

by introducing the shape function $\eta(z)$. Combining Eqs. (8) and Eq. (10) yields

$$Mc(z)q(z) = RR_0 \eta(z), \quad (11)$$

with the consistency condition $\eta(z_{ml}) = 1$. To derive the form of $\eta(z)$, we rely on the thermodynamic energy
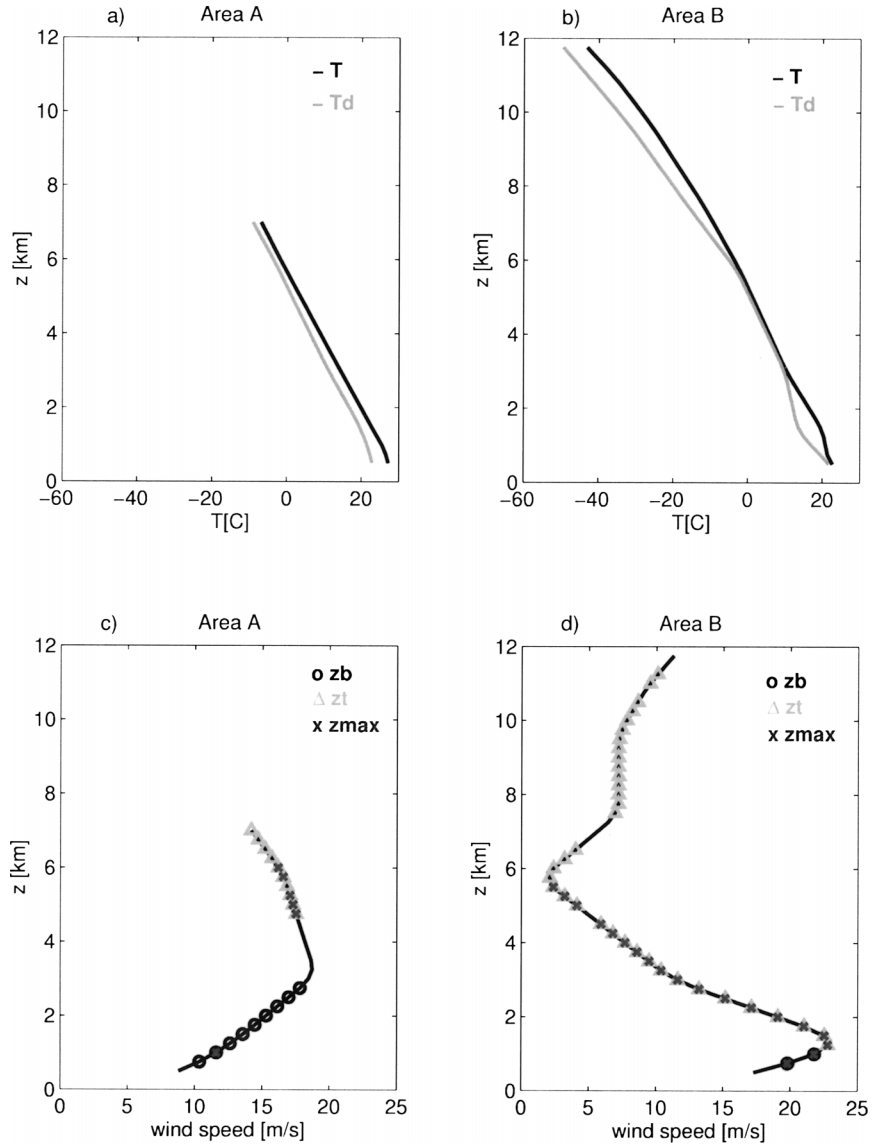
FIG. 4. Vertical profiles of the radiosondes located at the areas A and B on 17 Jun 1999. Distribution of cloud characteristics inferred from the PR reflectivity profiles (z_b, z_t, and z_{max}) is plotted along with the horizontal wind speed.

equation. Assuming small temperature fluctuations (e.g., in the Tropics), the thermodynamic energy equation can be expressed as an approximate balance between adiabatic cooling (left-hand side) and diabatic heating (right-hand side) below:

$$\omega^*(z)s(z) = -\frac{L_c}{C_p}\frac{dq_s(z)}{dt}, \qquad (12)$$

where $s(z)$ is the static stability, $\omega^*(z) = \omega(z)/\overline{H}$ is the vertical velocity in log pressure coordinates, $\overline{H}$ is the local-scale height, and q_s is the saturation mixing ratio. Considering the transformations ($d/dt = \omega\partial/\partial z$) and [$q(z) = q_s(z)\text{RH}(z)$], where $\text{RH}(z)$ is the relative humidity profile,

$$\omega^*(z)s(z) = -\frac{L_c}{C_p}\omega(z)\frac{\partial}{\partial z}\left[\frac{q(z)}{\text{RH}(z)}\right]. \qquad (13)$$

Equation (13) can be rewritten by combining Eqs. (11) and (12) as follows:

$$\omega^*(z)s(z) = -\frac{L_c}{C_p}\omega(z)\frac{\partial}{\partial z}\left[\frac{\text{RR}_0\eta(z)}{\rho(z)\omega(z)\text{RH}(z)}\right]$$

$$= -\frac{L_c}{C_p}\omega(z)\text{RR}_0\frac{\partial}{\partial z}\left[\frac{\eta(z)}{\text{Mc}(z)\text{RH}(z)}\right]. \qquad (14)$$

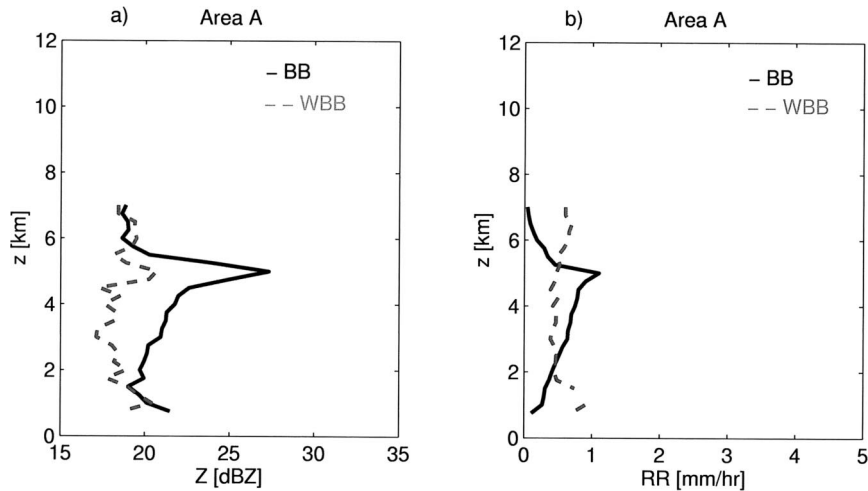Rearranging the terms, we finally obtain

FIG. 5. Vertical profiles of (a) the radar reflectivity and (b) the rain-rate estimates (TRMM PR 2A25 products) over area A on 17 Jun 1999—BB: data with brightband effect; WBB: data with brightband effect removed.

$$\frac{\partial}{\partial z}\left[\frac{\eta(z)}{\mathrm{Mc}(z)}\frac{1}{\mathrm{RH}(z)}\right] = -\frac{C_p}{L_c}\frac{\omega^*(z)}{\omega(z)}\frac{1}{\mathrm{RR}_0}s(z) \quad \text{and} \qquad (15\mathrm{a})$$

$$\left[\frac{\eta(z)}{\mathrm{Mc}(z)\mathrm{RH}(z)}\right]_{z_b}^{z} = -\frac{C_p}{L_c\mathrm{RR}_0}\left[-\int_{z_b}^{z}\frac{\omega^*(z)}{\omega(z)}s(z)\,dz\right]$$

$$= -\frac{C_p}{L_c\mathrm{RR}_0}\left[-\int_{z_b}^{z}\frac{s(z)}{\overline{H}}\,dz\right], \qquad (15\mathrm{b})$$

where $\mathrm{Mc}(z)$ is calculated according to Eq. (3) as in Stevens et al. (1977). Next, note that among the parameters in Eq. (3), all of the required pressure levels can be obtained normally from radiosonde data. The deep cloud mass flux, Mc_{ml}, is, therefore, the only unknown. However, our working premise is that moisture convergence takes place in the moist cloud layer, and, thus, $\mathrm{Mc}_{ml} = \overline{\rho}_{ml}\omega_{ml}$ (Stevens and Lindzen 1978; Yanai 1973).

To determine ω_{ml}, we further assume a thin well-mixed neutral boundary layer between the top of the moist layer (z_{ml}) and the top of the trade layer (z_{TR}), the depth of which is the same as the characteristic length of dominant eddies ($\omega' = U'$), and, thus,

$$\omega_{ml} = U_{TR} - U_{ml}, \qquad (16)$$

where U_{TR} and U_{ml} are the horizontal wind speeds at the trade level and at the top of the moist layer, respectively. The sign of ω_{ml} depends on the shape of the wind profile, but only positive values are used in our algorithm because we focus on the latent heating produced by updraft condensation.

Inspection of Eqs. (3), (5), and (11)–(15b) indicates that the latent heating is proportional to ω_0, the average value of the vertical velocity in the moist layer as per Chang (1976). However, while we are confident in the vertical behavior of the $\mathrm{LH}(z)$ predicted by Eq. (5), the lack of a dense network of vertical soundings that would allow us to derive an accurate estimate of the vertical

velocity at the scale of the TRMM PR footprint remains a challenge.

Ultimately, the systematic applicability of this approach hinges on its reliance on the vertical structure of TRMM PR reflectivity profiles to infer z_b and z_t, and rain-rate profiles to extract RR (z_{ml}) (Fig. 1a). The expected characteristics of the errors associated with this approximation are delineated in Fig. 1b: the shaded areas correspond to the errors that result from neglecting the latent heating contribution of the lower entrainment and top detrainment layers implied by using 18 dBZ as the rainfall detection threshold for the TRMM PR (see section 3c for further discussion). Although we anticipate that there will be other biases as compared with observations, especially in mountainous regions (Barros et al. 2000), one advantage of the proposed retrieval algorithm is that in the absence of direct observations we can rely on the evaluation work conducted for the PR algorithm to quantify rainfall uncertainty as compared with other sensors, or combined TMI PR retrievals.

A potential source of uncertainty in our algorithm is the lack of explicit consideration of the distinction between stratiform and convective rainfall. However, this distinction stems not from fundamental physics, but from the need to recognize differences in the vertical structure of latent heating at different stages in the life cycle of precipitating storms (Houze 1997). Despite relying originally on a cumulus parameterization of deep convection, none of the assumptions used in the cloud physics parameterization in the proposed algorithm implies one type of rainfall (and heating profile), or another. Furthermore, in contrast to algorithms that must infer the vertical structure of hydrometeor profiles to match radiometric observations, here the vertical structure is given by the function $\eta(z)$ constrained to the
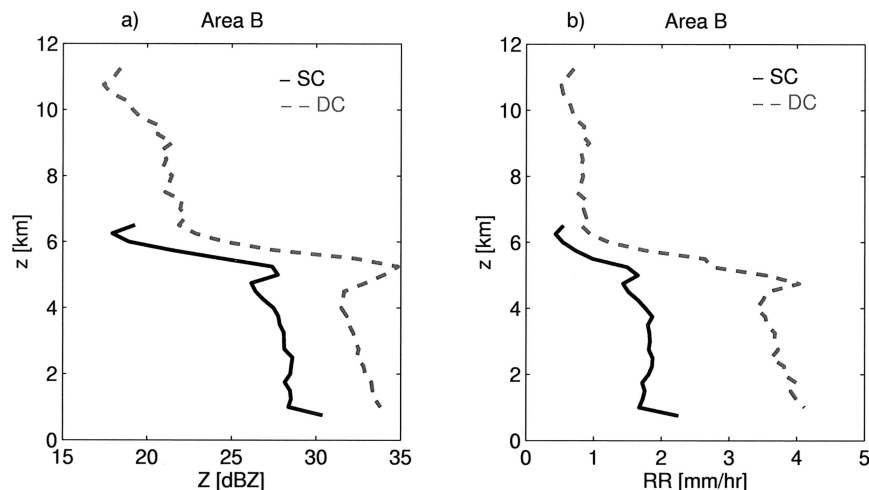
FIG. 6. Average vertical profiles of (a) the radar reflectivity and (b) the rain-rate estimates (TRMM PR 2A25 products) over area B on 17 Jun 1999. Here, shallow (SC) and deep clouds (DC) are distinguished according to the height of cloud top, respectively, below and above 6 km.

relationship between the integrated moisture and energy budgets in the cloud (the consistency condition) on the one hand, and the morphology parameters derived from the PR profile data on the other. Thus, the distinction between convective and stratiform systems is not necessary in the application of the algorithm.

The net evaporation cooling below the cloud base is estimated using the parameterization proposed by Barros and Lettenmaier (1994) to describe the thermodynamics associated with the interactions between descending hydrometeors and the surrounding environment. In the evaporative cooling scheme, the atmospheric column is divided in several layers, here defined with a vertical resolution consistent with that of TRMM PR data (250 m). Within each layer, the evaporative cooling $C(z)$ is assumed to be uniform and is calculated at the average height z_i,

$$C(z_i) = \begin{cases} \dfrac{L_v}{C_p} K_e v_e [e_{sat}(z_i) - e(z_i)] \\ \qquad z_s + 125 \text{ m} \leq z_i \leq z_b - 125 \text{ m} \\ 0 \qquad \text{elsewhere,} \end{cases} \quad (17)$$

where z_s and z_b are the surface and the cloud-base levels, respectively. Following Barros and Lettenmaier (1994), the efficiency of the vertical transport of water vapor K_e is taken as $K_e = 1.52 \times 10^{-4}$ cm km^{-1} hPa^{-1}, and v_e is an effective fall velocity of hydrometeors ($v_e \approx 7$ m s^{-1}).

3. Data description

Our study area is the region of the Indian subcontinent and Tibetan plateau (15°–32°N, 70°–95°E) surrounded by the Arabian Sea to the west, the Bay of Bengal to

the east, and the Tibetan plateau to the north (Figs. 2a,b). The TRMM PR 2A25 products (corrected reflectivity Z, and the rain-rate estimates) and radiosonde data for June of 1999, 2000, and 2001 were used to estimate the vertical profile of latent heating.

a. Satellite data

The TRMM PR is the first meteorological radar in space (Kummerow and Barnes 1998). It operates in the K band (13.8 GHz), with single polarization, a horizontal resolution of 4.3 km, and a vertical resolution of 250 m. Therefore, 80 vertical bins are available from 0 km up to a height of 20 km. The swath width is 215 km for the ±17° scan angle range. Each beamwidth is about 0.7°, resulting in 49 angle bins within one scan line. Further information on this sensor and on the data acquisition can be obtained on the Web site of TRMM (see online at http://trmm.gsfc.nasa.gov/overview_dir/pr.html).

Because the signal at 13.8 GHz is attenuated by rain, we use the 2A25 products (version 5.6) corrected for rain attenuation (Iguchi and Meneghini 1994). These are the corrected radar reflectivity (Z) and the rain rate (RR) estimated from an appropriate Z–R relationship. Although it is recognized that the algorithms for estimating the rain rates from the TRMM PR data may provide underestimated values (Kummerow et al. 2000), these estimates are used because of their fine spatial resolution. The retrieval algorithm used to generate the 2A25 products also removes the effects of surface clutter on the signal. Nevertheless, occasionally, the corrected radar reflectivity Z is below 0. In this case, both the reflectivity and rain rates are set to 0 in the algorithm. The data are also compared with terrain elevation ex-
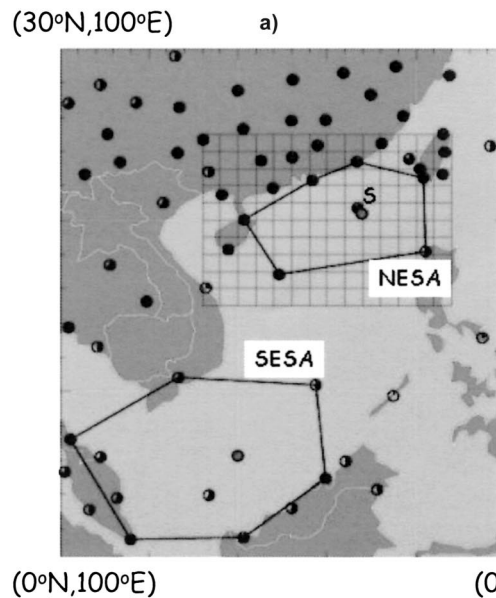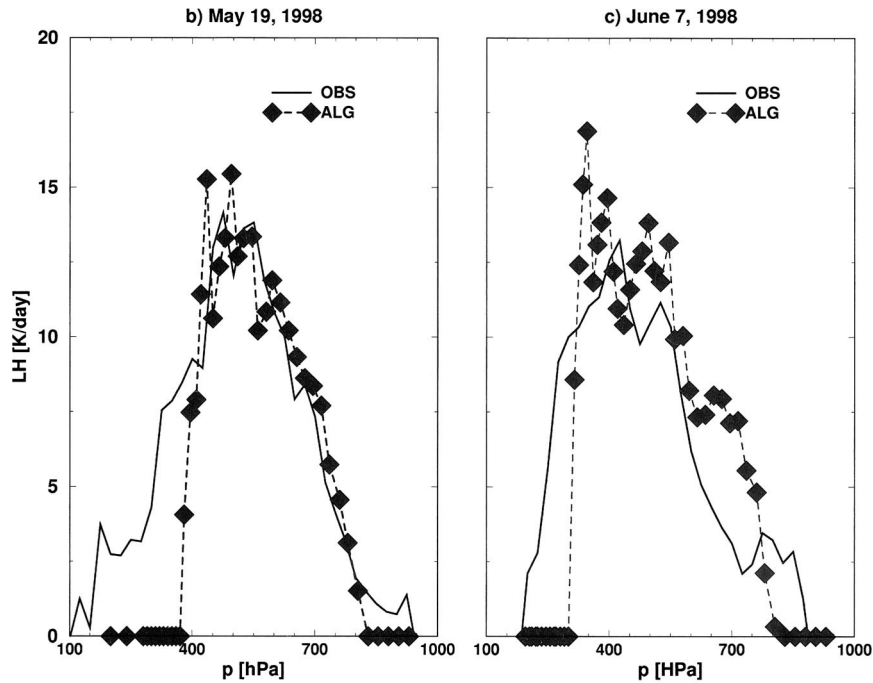
FIG. 7. Intercomparison between latent heating profiles derived from the analysis of radiosonde data during SCSMEX (OBS; Johnson and Ciesielski 2002) and estimated by the proposed algorithm using TRMM data (ALG) and radiosonde data at one central station [World Meteorological Organization (WMO) 2003]: (a) map showing the SCSMEX region, the radiosonde network, the geometry of the NESA polygon (northern enhanced array), and the location (S) of the radiosonde station that provided the data for the retrieval algorithm; (b) latent heating profiles for 19 May 1998 [OBS (0600 LST), TRMM overpass (0636–0807 LST)]; (c) latent heating profiles for 7 Jun 1998 [OBS (1200 LST), TRMM overpass (1316–1447 LST)]. The profiles correspond to gridded averages of radiosonde analysis over the SCSMEX NESA area in the case of OBS, and to averages over all the pixels within a TRMM overpass that meet the algorithm criteria with regard to the radiosonde station used for retrieval in the case of ALG. Details about SCSMEX are given by Johnson and Ciesielski (2002). (Data can be obtained online at http://updraft.atmos.colostate.edu/~scsmex.)

tracted from a digital elevation model to detect possible surface clutter effects. These cases, though rare, do occur in the northeastern portion of our domain (in the Tibetan plateau), and they were eliminated from consideration in the latent heating algorithm.

Overall, during June 1999, June 2000, and June 2001, there were, respectively, 179, 182, and 180 PR overpasses over the study area. These data were extracted directly from the TRMM Data Search and Order System (available online at http://lake.nascom.nasa.gov).

b. Radiosonde data

Figure 2a shows the spatial distribution of radiosondes over the study area, during June 1999. Because of the high horizontal and vertical variability of the atmospheric parameters over land and their close relationship with the atmospheric latent heating, the spatial coverage of the radiosondes is clearly insufficient for an accurate estimation of the spatial distribution of the vertical profile of latent heating over the entire area of
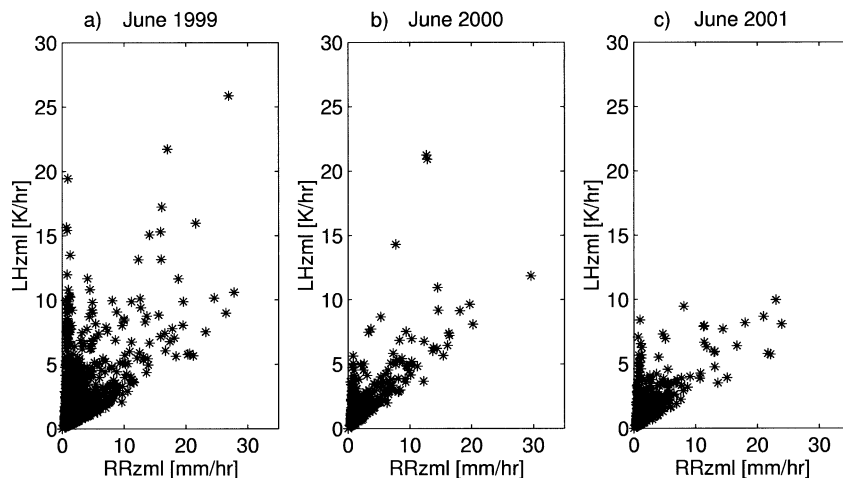
FIG. 8. Results of the parameterization at the top of the moist layer expressed in terms of LH(z_{ml}) vs RR(z_{ml}): (a) Jun 1999, (b) Jun 2000, and (c) Jun 2001.

study. In Fig. 2b, the plot of the radiosonde locations against the TRMM PR overpasses on 17 June 1999 illustrates the poor spatial match between the satellite path and the location of radiosonde stations.

The radiosonde data were obtained from the National Oceanic and Atmospheric Administration (NOAA) Forecast Systems Laboratory (FSL) and the National Climatic Data Center (NCDC) database (available online at http://raob.fsl.noaa.gov). There are 23, 29, and 27 radiosonde stations in the area delimited by 15°–32°N, 70°–95°E during June 1999 (Fig. 2a), June 2000, and June 2001, respectively. For each station, the surface and the mandatory levels were extracted and then processed. To combine the TRMM PR data and the radiosondes, it is necessary to interpolate the soundings with respect to the vertical resolution of the PR sensor (250 m).

The radiosonde and PR data were acquired at different time and spatial scales, which must be reconciled to run the algorithm. Inevitably, this is another source of uncertainty but is, however, necessary to increase the number of retrievals to a statistically meaningful level. Therefore, the synchronicity requirement is relaxed spatially by applying the retrieval algorithm to all pixels in the overpass that are within 50 km of the radiosonde location. With regard to timing, a threshold interval of 3 h around the radiosonde launching time is used for measurements that satisfy the spatial criterion. Because of the high variability of the atmospheric parameters, at times these conditions may be insufficiently restrictive, and, therefore, care should be taken in the interpretation of results.

In addition to the vertical, horizontal, and temporal criteria discussed above, the retrieval is conducted only if the cloud base is higher than the minimum level of the sounding acquisition. This additional constraint allows us to compute the vertical velocity at the cloud base from the radiosonde data as per Eq. (16). When all of these conditions are met, only 21, 14, and 20 TRMM overpasses are available for processing in 1999, 2000, and 2001 respectively. Table 1 provides a record of the data-pruning process as a result of the application of all the selection criteria. Figure 3 depicts the area covered by the TRMM PR overpasses and the radiosondes that are used to retrieve the latent heating profile during the period of study.

c. Extraction of relevant cloud parameters

The cloud base z_b, the top of the moist layer z_{ml}, and the cloud top z_t, are key parameters in the retrieval algorithm (Figs. 1a and 1b). Recently, Wilheit and Hutchison (2000) showed the possibility of estimating the cloud base from a combination of passive microwave and infrared satellite data. However, over land the results obtained from passive microwave data are strongly affected by surface emissivity (Kummerow et al. 1996). Although there are methods for determining the cloud base and the cloud top from radiosonde data (e.g., Chernykh and Eskridge 1996), our objective is to rely as little as possible on radiosonde data, and as much as possible on satellite data. Thus, the cloud base and the cloud top are extracted from the vertical profile of the radar reflectivity. The cloud base is taken to be the lowest level with the PR minimum detectable reflectivity of 18 dBZ or, in the case of intense rainfall 250 m (i.e., one level in terms of PR vertical resolution), below the level of the highest level where PR rainfall reaches its maximum. A comparison between the heights of cloud base determined according to this criterion and lifting condensation level (LCL) estimates at radiosonde locations in the Indian subcontinent agrees very well (with a coefficient of determination > 0.9). As mentioned earlier, Stevens et al. (1977) set the trade level p_{TRADE} 50 hPa above the cloud base. Following sensitivity analysis, we also use this value here.
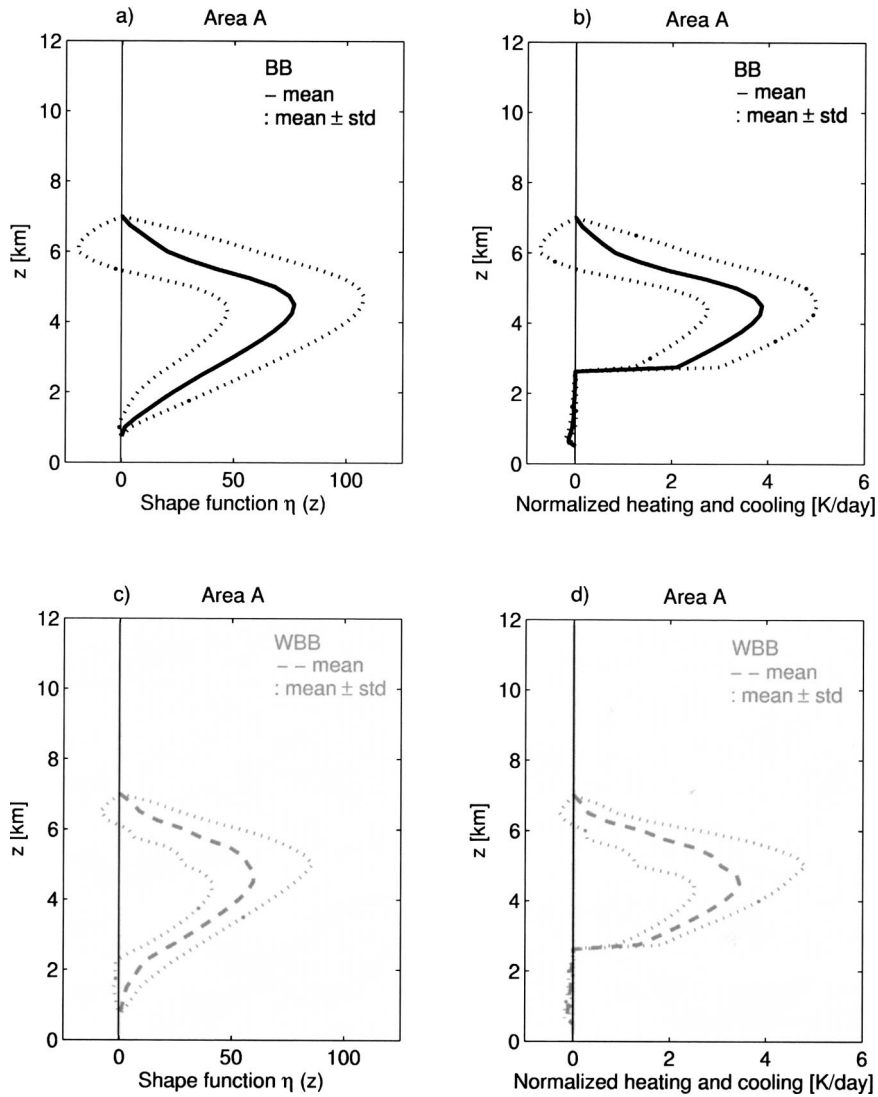
FIG. 9. (left) Mean vertical profiles of the shape function, $\eta(z)$, and (right) those of the normalized latent heating and cooling over area A on 17 Jun 1999 for (top) BB and (bottom) WBB.

In the algorithm, the cloud top is the highest level with a radar reflectivity value of 18 dBZ (Fig. 1a). Heymsfield et al. (2000) provide careful analysis of precipitation radar reflectivity profiles as compared with high-resolution airborne and ground-based radar measurements. They point out that the limited sensitivity of the PR implies that large portions of the upper regions of precipitating clouds will be undetected, especially in the case of stratiform rainfall (<0.4 mm h^{-1}) and in the ice regions of precipitating clouds (shaded area in Fig. 1b). They also point out that in the case of large precipitation systems (convective cells greater than the minimum resolution of the PR ≈ 18.5 km^2), the vertical structure of PR reflectivity profiles agrees very well with other radars, and that the PR accurately detects bright bands. In the Indian subcontinent, most precipitating systems are characterized by deep convection embedded in larger areas of relatively heavy rainfall (Barros et al. 2003). Monsoon systems associated with heavy rainfall on the Himalayan range exhibit a ''stratiformlike'' spatial structure with shallow embedded convection (the tops of orographic clouds remain generally below 500 hPa) and, thus, are morphologically similar in many respects to the more ubiquitous mesoscale convective systems but for cloud depth (Lang and Barros 2002). The problem of storm-height underestimation is revisited in section 3d, when we evaluate the algorithm against radiosonde analysis.

At the top of the moist layer z_{ml}, the cloud mass flux is very large because of cloud detrainment. In our algorithm, the moist layer is placed at the level of highest rainfall rate (Fig. 1a), consistent with the fact that the cloud mass flux reaches its maximum at the top of the moist layer (Yanai et al. 1973; Stevens et al. 1977).
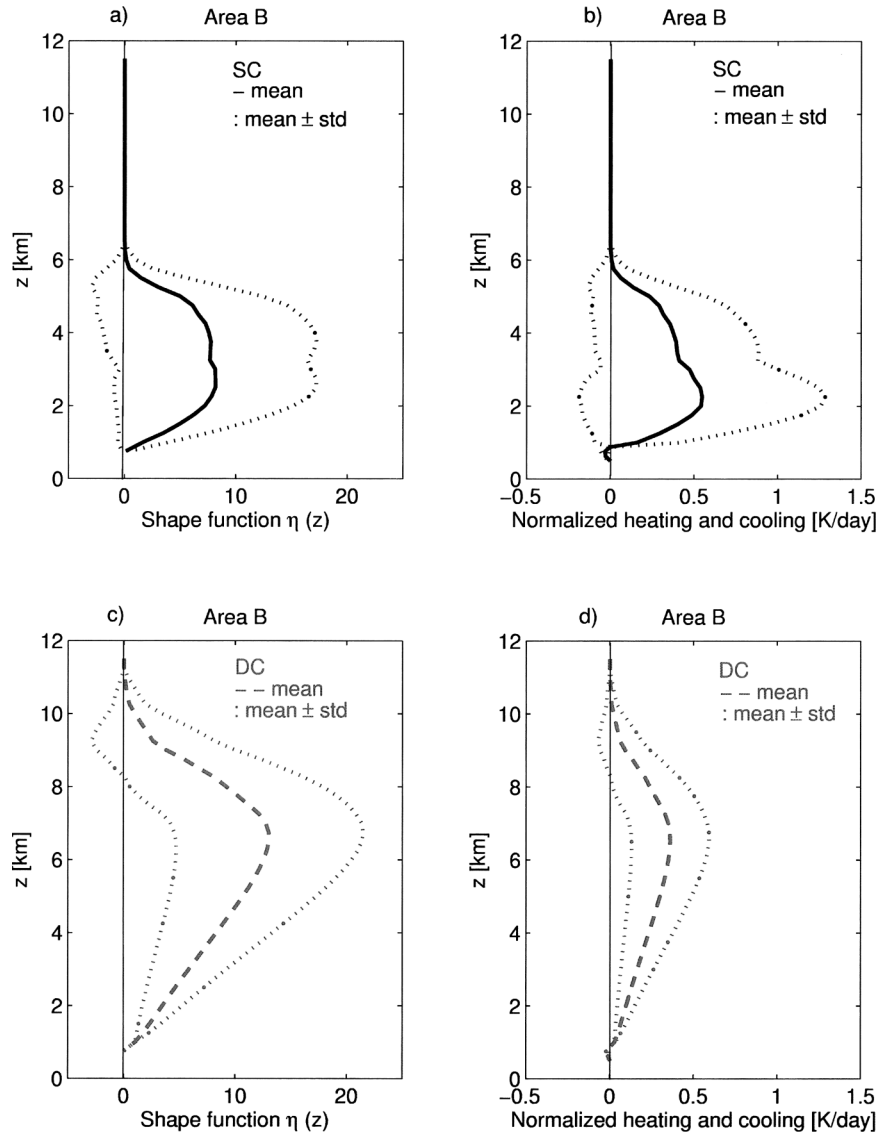
FIG. 10. Mean vertical profiles of the shape function, $\eta(z)$, and those of the normalized latent heating and cooling over area B on 17 Jun 1999 as in Fig. 9.

The radiosonde profiles of air temperature T, dewpoint T_d, and horizontal wind ($U = \sqrt{u^2 + v^2}$) are shown in Figs. 4a–d at locations A and B approximately 260 km from each other on 17 June 1999 (Fig. 2b). Marked in the Figs. 4c and 4d are the distributions of cloud base z_b, cloud top z_t, and the level of maximum PR reflectivity z_{max} for all pixels that match the algorithm criteria in the area of influence of each radiosonde. Figures 5 and 6 show characteristic profiles of TRMM PR 2A25 reflectivity and rain-rate estimates within the area of influence of each station. The atmosphere at A is significantly drier than at B, and the cloud-base levels as well as the cloud-top heights exhibit a wider range of variation at B. In fact, some of the reflectivity profiles include a "brightband" layer at 5-km altitude (marked as BB in Figs. 5a–b). Owing to the melting of ice par-

ticles, and, therefore, to the increase in the dielectric constant of the melting particles, this layer has much higher reflectivity than its surroundings, which has a significant impact on rainfall retrieval. Given the lower rain rates estimated in area A, we hypothesize that the scenario is consistent with the presence of a mixture of altostratus, stratocumulus, and nimbostratus. In the case of location B, we emphasize the presence of both deep (DC) and shallow (SC) clouds within the 50-km radius area of influence of the radiosonde station (Figs. 6a–b). Here, shallow and deep clouds are distinguished according to the height of cloud top, respectively, below and above 6 km. The difference in the depths of shallow and deep clouds is on the order of 4–5 km. The distributions of cloud-base, cloud-top, and maximum reflectivity heights at location B (Fig. 4d) indicate the pres-
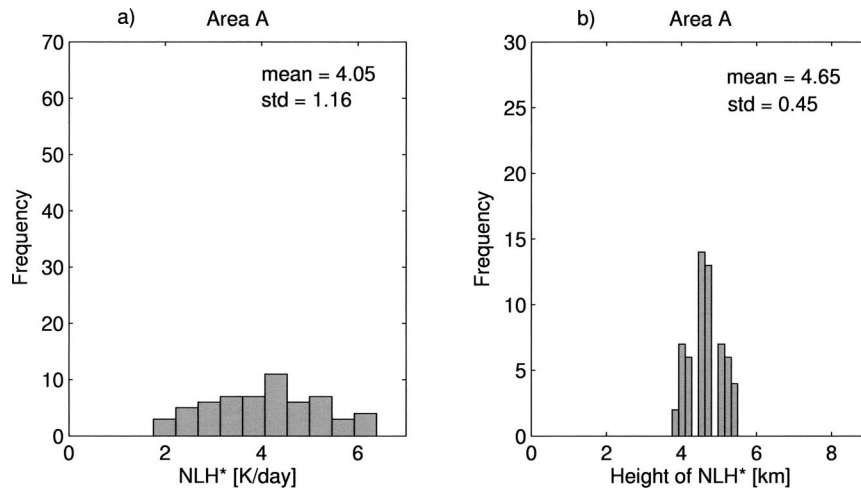
FIG. 11. Frequency distributions of (a) maximum heating [normalized by rain rate (1 cm day^{-1})] and (b) height over area A on 17 Jun 1999.

ence of a rather uniform cloud base at about a 1-km height above MSL, while there is a wide range of variation of cloud-top height (up to 12 km) and height of maximum reflectivity, suggesting a chaotic mixture of cumulonimbus, stratocumulus, and altocumulus clouds, consistent with the higher rain rates estimated in area B and with the presence of a bright band in the average profiles (Figs. 6a,b). Also, note the contrasting differences in wind profiles at A and B. The strong decrease in horizontal wind speeds with height at B as compared with A and the fact that this decrease occurs in a region (2.5–5 km) where the lower troposphere is completely saturated are consistent with the presence of towering cumulus and heavy rainfall.

d. Evaluation against SCSMEX analysis

The algorithm was evaluated against latent heating estimates from analysis of radiosonde data during the SCSMEX performed by Johnson and Ciesielski (2002) during the two intense observation periods between 5 May and 20 June 1998. Radiosonde data and latent heating profile estimates were obtained from Colorado State University (available online at http://updraft.atmos. colostate.edu/~scsmex). The retrievals were conducted using data from the Northern Enhanced Sounding Array (NESA) sounding station S3, Fig. 7a. Figures 7b,c show the comparison between 6-hourly latent heating profiles by Johnson and Ciesielski (2002) gridded and averaged over the NESA network area (marked as OBS), and the average of the profiles retrieved (marked as ALG) for two different overpasses during monsoon onset (9 May 1998; Fig. 7b) and postonset (7 June 1998; Fig. 7c). Given the inconsistency between TRMM overpass and radiosonde launching times, the OBS profile closer to the time of the overpass is used for comparison.

The results show good agreement of the ALG profiles with OBS profiles between 850 and 300 hPa. As ex-

pected, systematic differences are present in the upper and lower limbs of the profiles because of errors in extracting cloud top and cloud base from the PR reflectivity profile (see shadowed areas in Fig. 1b). Note that the underestimation of cloud-top height is the largest source of error, and its relative contribution may be particularly significant in the case of high clouds when ice microphysics play an important role in precipitation processes (e.g., stratiform rainfall). Because of the well-defined characteristics of the underestimation errors, there are several possible approaches to address this problem. For example, the 18-dBZ threshold cutoff at cloud top can be eliminated, and the shape of the reflectivity profile above the 18-dBZ level can be used to infer the shape of $\eta(z)$. Alternatively, a function such as that used in Eq. (3) can be used to interpolate between the level of maximum heating and Z^*, where LH(Z^*) = 0 (e.g., $Z^* = 14.5$ km; as in Augustin and Schmidt 1974 and Stevens et al. 1977). In this manuscript, we will not pursue these solutions, although they may be useful for generating latent heating data products operationally.

Last, although the SCSMEX diagnostics may be strongly affected by sampling errors (P. Ciesielski 2003, personal communication), they provide a reference to assess the utility of the proposed algorithm. Specifically, this study suggests that the algorithm captures well the magnitude and functional behavior of the latent heating profiles between the moist layer and the level of maximum heating.

4. Systematic retrieval products

The magnitude of the radar reflectivity Z measured by the PR sensor is directly proportional to the sixth power of hydrometeor diameter, independent of the process that leads to the growth of the droplets. However, the atmospheric latent heating, LH, resulting from the
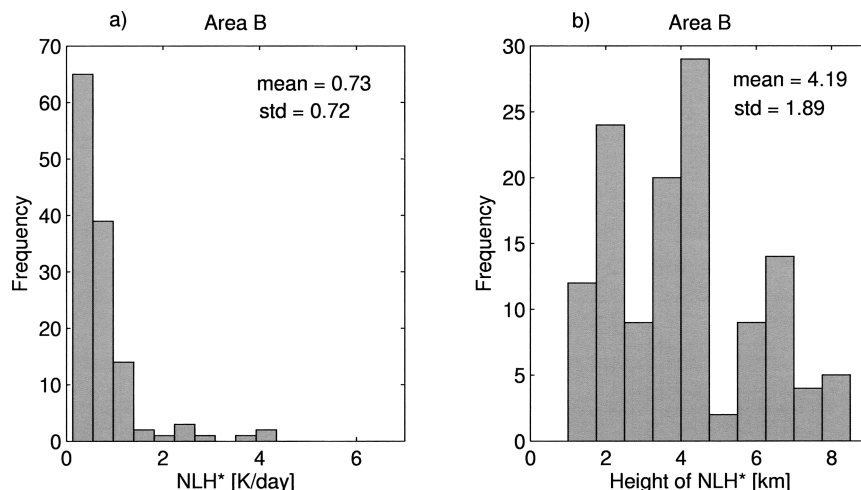
FIG. 12. Frequency distributions of the (a) maximum heating [normalized by rain rate (1 cm day^{-1})] and (b) height over area B on 17 Jun 1999.

condensation of moist air is not exclusively related to the vertical distribution of the hydrometeors, but also depends on dynamical processes in the cloud environment. Because of the difference in the physical content of these two variables, a direct Z–LH relationship is not necessarily observed (Cartwright and Ray 1999). As per Stevens et al. (1977), the rain rate and the latent heating are only related within the moist layer, and a Z–LH relationship is expected at the top of the moist layer. Above the z_{ml}, the heating is expressed as a function of cloud depth. Accordingly, Figs. 8a–c show a positive relationship between the atmospheric latent heating and the rain rate at the top of the moist layer. Note that for heating rates above 10 K h^{-1}, there is significant scatter. These points correspond to locations where midlevel and deep clouds occur, and, therefore, the presence of ice particles becomes important relative to the water droplets.

a. Tests of algorithm consistency

The shape function $\eta(z)$, and the normalized latent heating and cooling profiles NLH(z) and NC(z) [i.e., latent heating and cooling per unit rainfall (1 cm day^{-1})] are computed according to Eqs. (15b), (5), and (17), respectively. Selected cases are shown in Figs. 9 and 10 for the overpass of the TRMM PR on 17 June 1999 assigned to the radiosondes acquired at 1100 and 1200 UTC at the two coastal locations A and B (Figs. 2b, 4, 5, and 6). In comparison with the latent heating, no significant evaporative cooling is noticed.

Because the physical processes associated with the presence of the bright band are not included in convective parameterizations in general (Houze 1997), and in this one in particular, reflectivity profiles with bright-band effects should in principle not be included in latent heating estimates. Retrievals using reflectivity profiles with BB and without bright band (WBB) are shown in

Fig. 9 for location A. There is a difference on the order of 0.5 K day^{-1} between the two cases.

Equations (12b) and (16) indicate that while $\eta(z)$ is directly proportional to the cloud mass flux, NLH(z) is related to the ratio of the latter to the cloud depth. Accordingly, although $\eta(z)$ and NLH(z) exhibit a similar vertical structure, their magnitudes are not linearly related, and NLH(z) also depends on cloud depth as shown in Fig. 10 for shallow and deep clouds at location B.

A difference of about a factor of 4–5 can be observed between the mean values of the maximum latent heating of the two areas (cf. Figs. 9 and 10). The stratification of the retrieved profiles at location B into deep and shallow clouds (Fig. 10) shows that the disparity between the range of estimated latent heating at A and B cannot be explained by cloud depth. An inspection of $\eta(z)$ indicates that, in the algorithm, the difference can be attributed to the vertical velocity, which is to say the cloud mass flux at midlevels in area A. As suggested by our previous discussion in the context of Figs. 4, 5, and 6, these discrepancies result from the diversity of cloud characteristics in each region, and resemble the differences reported by previous authors between convective and stratiform rainfall albeit in other environments and coarser spatial resolution (see, e.g., discussion in Gallus and Johnson 1991). Nevertheless, caution must be exercised in the interpretation of latent heating profiles for stratiform rainfall (high and midlevel clouds where ice microphysics are relevant).

An overview of the statistics of the maximum values of normalized latent heating in regions A and B is given in Figs. 11 and 12, respectively. For the first location (area A, Fig. 11), the maximum value of the normalized latent heating (NLH*) varies from 2 to 6 K day^{-1} per unit rainfall (1 cm day^{-1}) with a mean value of 4.0 K day^{-1} at 4.6 km; for the second (area B, Fig. 12), values are obtained in the 0–4 K day^{-1} range, with a mean of
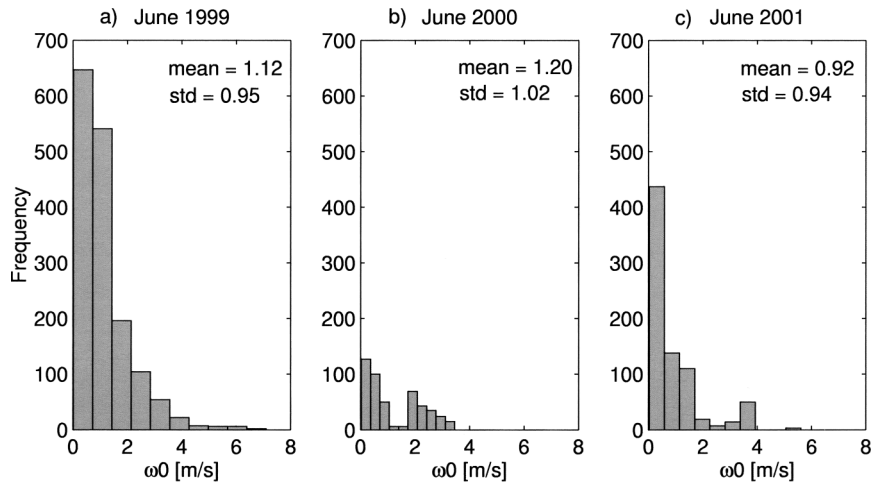
FIG. 13. Frequency distributions of the estimated vertical velocity at cloud base (a) Jun 1999, (b) Jun 2000, and (c) Jun 2001.

0.7 K day^{-1} at 4.2 km. Note that there is a much larger number of overpass pixels that met the retrieval criteria at location B than at location A, and, therefore, our results in Figs. 11 and 12 may be somewhat biased by the lack of enough data to fully contrast the variability in the two regions.

The vertical velocity ω_0, necessary to compute the cloud mass flux Mc [Eq. (3)], is derived from Eq. (16). For terrain elevations below 2000 MSL, the frequency distribution gives mean values of 0.80, 1.13, and 0.86 m s^{-1} for June 1999, 2000, and 2001, respectively (Figs. 13a–c). High interannual variability, however, is attributed to the variability in the vertical profile of the horizontal wind speed used to compute ω_0. Over the Indian subcontinent, the vertical velocity is smaller than 4 m s^{-1}, and in the Tibetan plateau (not shown) it reaches 6 m s^{-1}.

While the maximum value of the normalized latent heating, NLH*, shows values smaller than 8 K day^{-1} for June 1999 and 2000, the range of variation is between 0 and 10 K day^{-1}, for June 2001. These results are consistent with differences in regional large-scale convective activity among 1999, 2000, and 2001 (Lang and Barros 2002; Barros and Lang 2003). Nevertheless, one must be careful in interpreting interannual variability from these data, given the large discrepancy in the number of retrievals in 1999 as compared with 2000 and 2001 (Table 1). The average maximum heating values during the 3 months studied range between 1.3 and 1.6 K day^{-1} (Figs. 14a–c). Considering the height of the maximum latent heating, the frequency distribution (Figs. 14d–f) gives mean values of 5.7 ± 2, 3.8 ± 1.5, and 4.8 ± 1.7 km MSL, respectively, for June 1999, 2000, and 2001. (These values are higher than those in Table 2, because profiles for all locations were used in deriving the frequency distributions.) Note the mixture of deep convective and high stratiform clouds with the

height of NLH* well above 6 km as in Cartwright and Ray (1999).

Figures 15a–c show the maximum values of the normalized cooling (NC*) obtained for June 1999, 2000, and 2001. This analysis confirms the very low magnitude of evaporative cooling (less than 0.1 K day^{-1} on average) as in areas A and B (Figs. 7 and 8). The average height of maximum cooling is about 1 km MSL for June of the 3 yr (Figs. 15d–f).

Next, we compare our results with those obtained by Tao et al. (2001) over continental regions using the TRMM PR rain-rate estimates. From the monthly mean latent heating profiles over Africa, Australia, and South America, Tao et al. (2001) obtained a maximum heating located between 6 and 7 km using the convective–stratiform heating (CSH) PR algorithm. Using the TMI rainfall products in two other heating algorithms, the hydrometeor heating (HH) algorithm and the Goddard profiling (GPRO) algorithm, the same authors obtained two distinct maxima over continental regions: one in the 3–5-km layer, and another in the 6–7-km layer. This range of variability is consistent with the spread of our results in the Indian subcontinent as shown in Figs. 14d–f. For the magnitude of maximum heating, Tao et al. (2001) obtained values up to 10 K day^{-1} per unit of rainfall, with average values below 1 K day^{-1} in Africa and Australia, and slightly above 2 K day^{-1} in South America. Our estimates compare well with their results (Figs. 14a–c), although with higher averages than in Africa and Australia, consistent with heavier surface rainfall during the monsoon. Similarly to Tao et al. (2001), maximum cooling in our application to the Indian subcontinent remains below 2 km and generally does not exceed 0.2 K day^{-1} per unit rainfall (Figs. 15a–f).

To confirm the compatibility of our assumptions with regard to Stevens et al. (1977), we compare the results of this parameterization using the TRMM PR data with
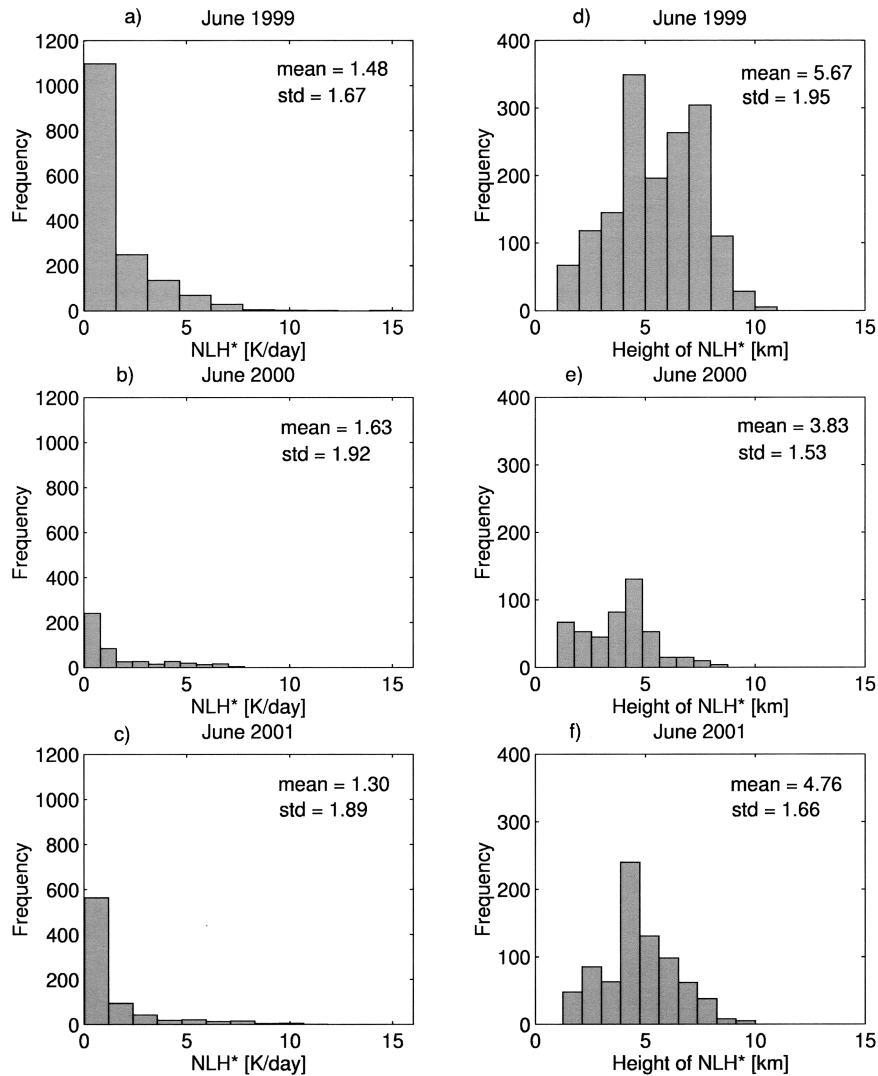
FIG. 14. Frequency distributions of (left) the maximum heating [normalized by rain rate (1 cm day^{-1})] and (right) height of the NLH*, respectively: (a) and (d) Jun 1999, (b) and (e) Jun 2000, and (c) and (f) Jun 2001.

those obtained via independent calibration against the radiosonde data. Figures 16a–c show a close agreement is obtained at the top of the moist layer, with a determination coefficient of about 0.9 for each of the 3 months. This result is important because it suggests that the algorithm may be applied in regions of deep convection where only PR data are available, such as are anticipated when we generalize the algorithm spatially.

b. Spatial and temporal variability

The results of vertical velocity ω_0 and the height and magnitude of maximum latent heating NLH* for terrain elevations below 2 km MSL in the Indian subcontinent are examined in Table 2, separating the early morning from the late afternoon cases. The mean values of the maximum latent heating and the vertical velocity are higher in the early morning (2300–0100 UTC, 0500–0700 LST) than in the late afternoon (1100–1200 UTC, 1700–1800 LST) for the 3 months studied. Interannual variability, especially with regard to late afternoon characteristics, is also high.

The signature of solar forcing in midafternoon convection in the Tibetan plateau is expected to be significant (Luo and Yanai 1983, 1984). Unfortunately, there were only two locations where the radiosonde data met the algorithm criteria (areas 8 and 9 in Fig. 3). Furthermore, late afternoon radiosonde data are only available for June 1999. It is, therefore, difficult to clearly distinguish morning versus afternoon heating profiles in the Tibetan plateau. Nevertheless, a comparison of Figs. 17 and 18 shows that the afternoon latent heating in the two plateau locations (areas 8 and 9) is at least of the same order of magnitude as that in the early morning.
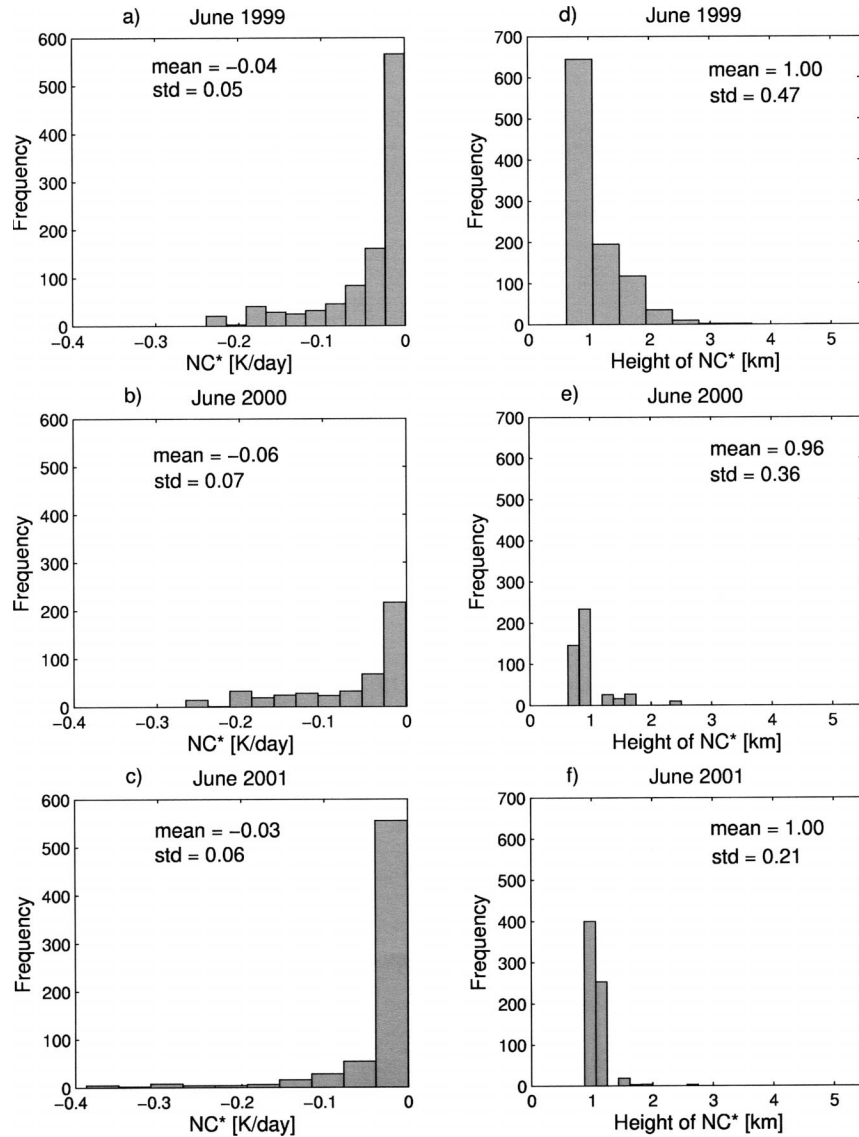
FIG. 15. Frequency distributions of (left) the maximum cooling [normalized by rain rate (1 cm day^{-1})] and (right) height of the NC*, respectively: (a) and (d) Jun 1999, (b) and (e) Jun 2000, and (c) and (f) Jun 2001.

The plateau is on average 4000 m above the Gangetic Plains in northern India where the other radiosondes (1–7) are stationed, and, therefore, the latent heating profiles are limited to an elevated layer of the troposphere (500–250 hPa) as compared with the corresponding profiles (900–500 hPa) on the southern edge of the Himalayan range. The profiles indicate that deep convection develops in the afternoon at locations 2–6, consistent with diurnal forcing by solar heating.

The diurnal cycle of the height and magnitude of maximum latent heating (the average of all retrievals in Table 2 for each year) were plotted as a function of the time of day in Fig. 19. Although the data are insufficient for conclusive inference, Fig. 19 does show that higher values of NHL* were observed at late night and early morning, in agreement with ground observations of heavier rainfall along the foothills of the Himalayas at the same time of day (Barros and Lang 2003; Barros et al. 2003). The early morning and late afternoon behavior is analyzed separately for locations 2 and 8, respectively, in northeast India and on the Tibetan plateau in the same figure (see Fig. 3 for location). In area 2, the magnitude of the afternoon peak is lower than the morning peak (0.5–1 K day^{-1} difference), but it develops 1–2 km higher in the troposphere. In area 8, there is an increase in z_{NLH*} in the afternoon but no significant difference in NLH*. Note also that there is a significant difference in afternoon values between 1999 and 2001, with higher NLH* and higher z_{NLH*} in 2001. Similar results were obtained at other stations, thus, suggesting that on av-
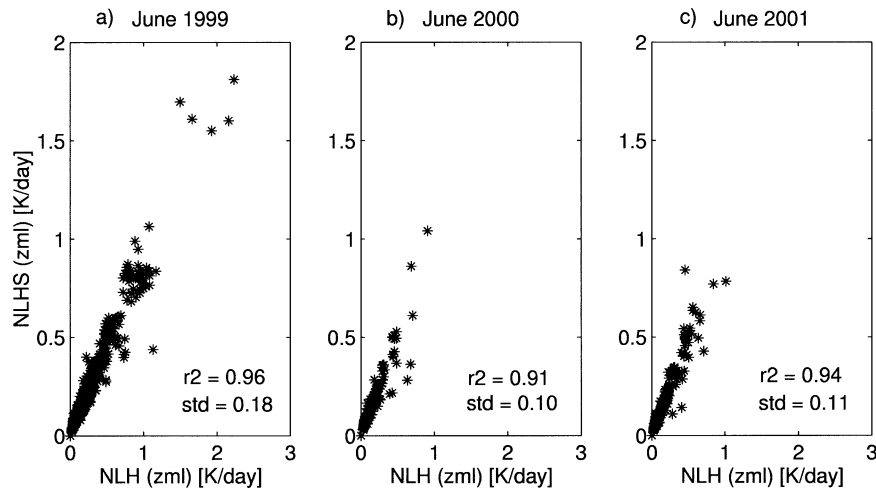
FIG. 16. Comparison between the normalized heating $NLH(z_{ml})$ obtained from the present parameterization and $NLHS(z_{ml})$ obtained following Stevens et al. (1977): (a) Jun 1999, (b) Jun 2000, and (c) Jun 2001.

erage the vertical structure of retrieved latent heating reflects the interannual variability of monsoon dynamics in the region. Overall, these results are encouraging because they are consistent with the analysis of convective activity from infrared and TMI imagery of cloud cover and rainfall observations (Lang and Barros 2002; Barros et al. 2003).

5. Discussion and conclusions

This study is an application of TRMM PR data to infer the vertical profile of the latent heating of precipitation. Cloud characteristics and the rain-rate estimates are extracted from TRMM PR 2A25 products. They are used with the basic equations of thermodynamic equilibrium and the parameterization of cloud mass flux to

TABLE 2. Results of vertical velocity, ω_0, and the location z_{NLH*} and magnitude of maximum latent heating, $NLH*$ for terrain elevations below 2000 m MSL (std dev refers to standard deviation).

Months	Parameters	Late afternoon	Early morning
Jun 1999	$\overline{\omega}_0$ (m s^{-1})	0.77	0.84
	Std dev (ω_0)	0.54	0.65
	$\overline{NLH}*$ (K day^{-1})	1.02	1.10
	Std dev ($NLH*$)	1.32	1.54
	$\overline{z}_{NLH*}$ (km)	4.23	5.15
	Std dev (z_{NLH*})	1.42	1.44
Jun 2000	$\overline{\omega}_0$ (m s^{-1})	0.82	1.37
	Std dev (ω_0)	0.80	1.02
	$\overline{NLH}*$ (K day^{-1})	0.68	2.32
	Std dev ($NLH*$)	0.80	2.20
	$\overline{z}_{NLH*}$ (km)	3.29	4.01
	Std dev (z_{NLH*})	1.42	1.28
Jun 2001	$\overline{\omega}_0$ (m s^{-1})	0.47	0.94
	Std dev (ω_0)	0.60	0.96
	$\overline{NLH}*$ (K day^{-1})	0.89	1.28
	Std dev ($NLH*$)	1.15	2.08
	$\overline{z}_{NLH*}$ (km)	5.12	4.30
	Std dev (z_{NLH*})	2.25	1.25

derive a simple expression of the vertical profile of atmospheric latent heating. The present work stems principally from the interest in the use of the TRMM PR data to investigate the vertical profile of the latent heating of precipitation over continental regions, because a number of studies have already focused on the retrieval of latent heating over the oceans. In addition, most studies based on satellite data were conducted with passive microwave data (e.g., SSM/I), and much fewer used active microwave spaceborne data (Tao et al. 2001).

Here, we propose a semiheuristic approach to reduce the complexity of the latent heating retrieval problem combining models (e.g., cloud parameterizations) and merging data (radiosonde, TRMM PR). Case studies of the results derived from two TRMM PR overpasses on 17 June 1999, show a difference of about a factor of 5 between the mean values of the maximum latent heating for two overpasses separated by a 260-km distance. Interannual analyses were also conducted for June of 1999, 2000, and 2001. The mean values of maximum latent heating normalized by unit rainfall depth (1 cm day^{-1}) during June 1999, 2000, and 2001 are equal to 1.5 ± 1.7, 1.6 ± 1.9, and 1.3 ± 1.9 K day^{-1}, respectively. The high variability observed on monthly results is explained by the spatial and temporal variability of both cloud properties and atmospheric parameters during each month. Latent heating maxima are located at 5.7 ± 2, 3.8 ± 1.4, and 4.4 ± 1.5 km MSL for June 1999, June 2000, and June 2001, respectively. While the level of the maximum heating is within the range obtained by Tao et al. (2001), over three continental regions, the range of variation of the maximum heating value is larger because of the higher values of rainfall rates observed over our study area. Results show no significant cooling, with a maximum located at about 1 km MSL for June 1999, June 2000, and June 2001. Although systematic retrievals were conducted only
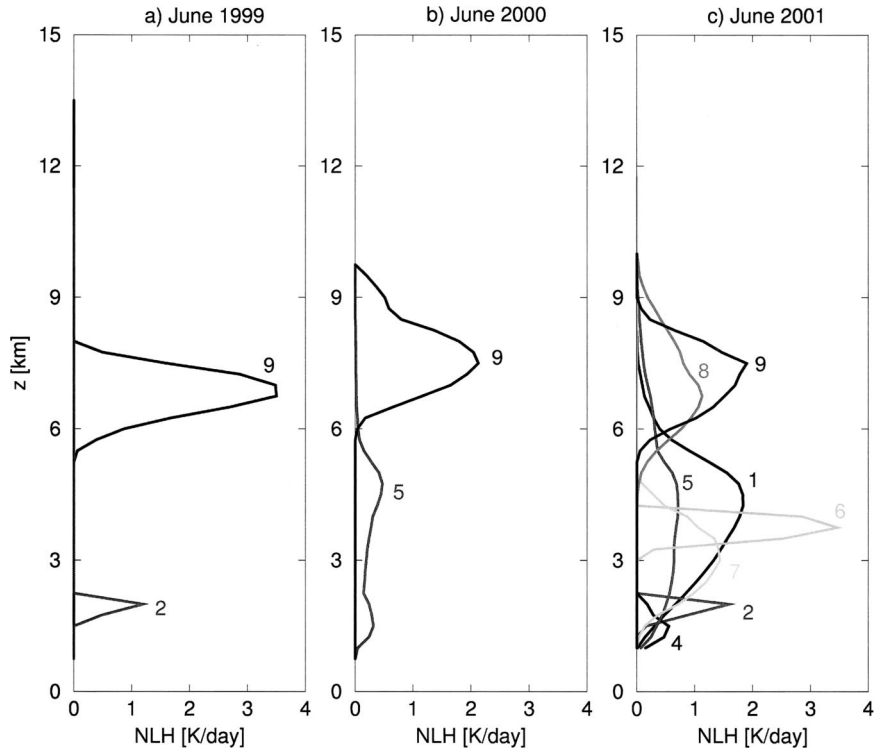
FIG. 17. Mean vertical profiles of normalized latent heating NLH(z) for areas 1–9 (see Fig. 2 for location) in the early morning: (a) Jun 1999, (b) Jun 2000, and (c) Jun 2001.
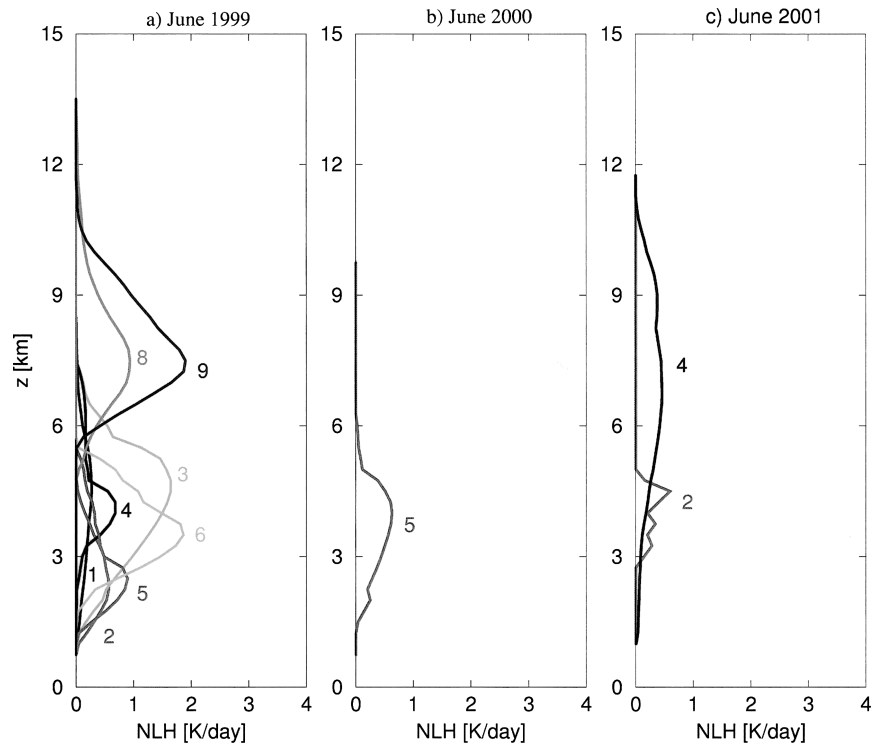

FIG. 18. Mean vertical profiles of normalized latent heating NLH(z) for areas 1–9 (see Fig. 2 for location) in the late afternoon: (a) Jun 1999, (b) Jun 2000, and (c) Jun 2001.
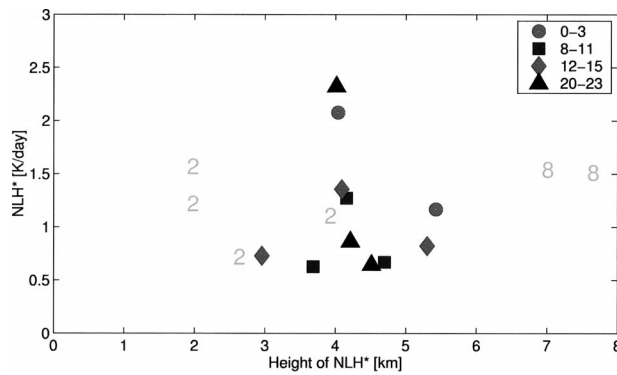
F_{IG}. 19. Diurnal cycle of maximum heating vs height for areas 1–7 (see Fig. 2 for locations) plotted as a function of time of day (0000–3000, 0800–1100, 1200–1500, and 2000–2300 LST). Also marked are the average morning and afternoon for areas 2 (south of the Himalayan range) and 8 (on the Tibetan plateau) during Jun of 1999 and 2001.

during June, the analysis of average profiles suggests that there is potential for high interannual variability in the vertical structure of latent heating in the Indian subcontinent, especially in the afternoon.

Along the southern-facing slopes of the Himalayas, the analysis of the evolution of the maximum value of the normalized latent heating shows higher values during the night and early morning than during the afternoon. This trend is consistent with the diurnal evolution of rainfall, convective available potential energy (CAPE), and precipitable water in the region of central Nepal, where ground-based observations exist (Barros et al. 2000; Barros and Lang 2003). A marked difference between the vertical structure of latent heating in the Indian subcontinent and on the plateau shows the impact of the Himalayan range in establishing a steplike singularity in the latitudinal distribution of latent heating in the extratropics during the monsoon.

Because of both spatial and temporal sampling inconsistencies between radiosonde data and TRMM overpasses, systematic evaluation of the algorithm should be conducted for a location where model results are available on a routine basis, such as, for example, the continental United States, where we can make use of existing radiosondes, as well as model-produced latent heating profiles. Errors associated with the cloud parameterization used in the algorithm can be characterized using synthetic cases generated via a cloud-resolving model and a radar algorithm. This is ongoing work. Further work is also needed to identify spatial organization patterns and functional relationships that may allow us to implement a spatial version of this algorithm at locations where radiosonde data are not available.

REFERENCES

Adler, R. F., G. J. Huffman, D. T. Bolvin, S. Curtis, and S. Nelkin, 2000: Tropical rainfall distribution determined using TRMM combined with other satellite and rain gauge information. *J. Appl. Meteor.,* **39,** 2007–2023.

Aonashi, K., and G. Liu, 2000: Passive microwave precipitation retrieval using TMI during the Baiu period of 1998. Part I: Algorithm description and validation. *J. Appl. Meteor.,* **39,** 2024–2037.

Augustin, E., and H. Schmidt, 1974: The vertical structure of the atmospheric planetary boundary layer in undisturbed trade winds over the Atlantic Ocean. *Bound.-Layer Meteor.,* **6,** 129–150.

Barros, A. P., and D. P. Lettenmaier, 1994: Introduction of a very simple evaporative cooling scheme into a dynamic model of precipitation efficiency in mountainous regions. *Mon. Wea. Rev.,* **122,** 2777–2783.

——, and T. J. Lang, 2003: Monitoring the monsoon in the Himalayas: Observations in central Nepal, June 2001. *Mon. Wea. Rev.,* **131,** 1408–1427.

——, M. Joshi, J. Putkonen, and D. W. Burbank, 2000: A study of the 1999 monsoon rainfall in a mountainous region in central Nepal using TRMM products and raingauge observations. *Geophys. Res. Lett.,* **27,** 3683–3686.

——, G. Kim, E. Williams, and S. Nesbitt, 2003: Probing landform–atmosphere interactions in the Himalayas and northern India during the monsoon. *Nat. Hazards Earth Syst. Sci.,* in press.

Cartwright, T. J., and P. S. Ray, 1999: Radar-derived estimates of latent heating in the subtropics. *Mon. Wea. Rev.,* **127,** 726–742.

Chang, C.-P., 1976: Vertical structure of tropical waves maintained by internally-induced cumulus heating. *J. Atmos. Sci.,* **33,** 729–739.

Chernykh, I. V., and R. Eskridge, 1996: Determination of cloud amount and level from radiosonde soundings. *J. Appl. Meteor.,* **35,** 1362–1369.

Gallus, W., Jr., and R. H. Johnson, 1991: Heat and moisture budgets of an intense midlatitude squall line. *J. Atmos. Sci.,* **48,** 122–146.

Halverson, J., M. Garstang, J. Scala, and W.-K. Tao, 1996: Water and energy budgets of a Florida mesoscale convective system: A combined observational and modeling study. *Mon. Wea. Rev.,* **124,** 1161–1180.

Hartman, D. L., H. H. Hendon, and R. A. Houze Jr., 1984: Some implications of the mesoscale circulation in tropical cloud clusters for large-scale dynamics and climate. *J. Atmos. Sci.,* **41,** 113–121.

Heymsfield, G. M., B. Geerts, and L. Tian, 2000: TRMM precipitation radar reflectivity profiles as compared with high-resolution airborne and ground-based radar measurements. *J. Appl. Meteor.,* **39,** 2080–2102.

Holton, J. R., 1979: *An Introduction to Dynamic Meteorology.* 2d ed. Academic Press, 391 pp.

Houze, R. A., Jr., 1982: Cloud clusters and large-scale vertical motions in the Tropics. *J. Meteor. Soc. Japan,* **60,** 396–410.

——, 1989: Observed structure of mesoscale convective systems and implications for large-scale heating. *Quart. J. Roy. Meteor. Soc.,* **115,** 425–461.

——, 1997: Stratiform precipitation in regions of convection: A meteorological paradox? *Bull. Amer. Meteor. Soc.,* **78,** 2179–2196.

Iguchi, T., and R. Meneghini, 1994: Intercomparison of single frequency methods for retrieving a vertical rain profile from air-

borne or spaceborne radar data. *J. Atmos. Oceanic Technol.,* **11,** 1507–1516.

Johnson, R. H., 1982: Vertical motion of near-equatorial winter monsoon convection. *J. Meteor. Soc. Japan,* **60,** 682–690.

——, and P. E. Ciesielski, 2002: Characteristics of the 1998 summer monsoon onset over the northern South China Sea. *J. Meteor. Soc. Japan,* **80,** 561–578.

Krishnamurti, T. N., and H. H. Bhalme, 1976: Oscillation of a monsoon system. Part I: Observational aspects. *J. Atmos. Sci.,* **33,** 1515–1541.

Kummerow, C., and W. Barnes, 1998: The Tropical Rainfall Measuring Mission (TRMM) sensor package. *J. Atmos. Oceanic Technol.,* **15,** 809–817.

——, W. S. Olson, and L. Giglio, 1996: A simplified scheme for obtaining precipitation and vertical hydrometeor profiles from passive microwave sensors. *IEEE Trans. Geosci. Remote Sens.,* **34,** 1213–1232.

——, and Coauthors, 2000: The status of the Tropical Rainfall Measuring Mission (TRMM) after two years in orbit. *J. Appl. Meteor.,* **39,** 1965–1982.

Lang, T. J., and A. P. Barros, 2002: An investigation of the onsets of the 1999 and 2000 monsoons in central Nepal. *Mon. Wea. Rev.,* **130,** 1299–1316.

Lau, K.-M., and L. Peng, 1987: Origin of low-frequency (intraseasonal) oscillations in the tropical atmosphere. Part I: Basic theory. *J. Atmos. Sci.,* **44,** 950–972.

Luo, H., and M. Yanai, 1983: The large-scale circulation and heat sources over the Tibetan plateau and surrounding areas during the early summer of 1979. Part I: Precipitation and kinematic analyses. *Mon. Wea. Rev.,* **111,** 922–944.

——, and ——, 1984: The large-scale circulation and heat sources over the Tibetan plateau and surrounding areas during the early summer of 1979. Part II: Heat and moisture budgets. *Mon. Wea. Rev.,* **112,** 966–989.

Olson, W. S., C. Kummerow, H. Hong, and W.-K. Tao, 1999: Atmospheric latent heating distributions in the Tropics derived from satellite passive microwave radiometer measurements. *J. Appl. Meteor.,* **38,** 633–664.

Stevens, D. E., and R. S. Lindzen, 1978: Tropical wave-CISK with a moisture budget and cumulus friction. *J. Atmos. Sci.,* **35,** 940–961.

——, ——, and L. J. Shapiro, 1977: A new model of tropical waves incorporating momentum mixing by cumulus convection. *Dyn. Atmos. Oceans,* **1,** 365–425.

Sui, C.-H., and K.-M. Lau, 1989: Origin of low-frequency (intraseasonal) oscillations in the tropical atmosphere. Part II: Structure and propagation of mobile wave-CISK modes and their modification by lower boundary forcings. *J. Atmos. Sci.,* **46,** 37–56.

Tao, W.-K., J. Simpson, S. Lang, M. McCumber, R. Adler, and R. Penc, 1990: An algorithm to estimate the heating budget from vertical hydrometeor profiles. *J. Appl. Meteor.,* **29,** 1232–1244.

——, S. Lang, J. Simpson, and R. Adler, 1993: Retrieval algorithms for estimating the vertical profiles of latent heat release: Their applications for TRMM. *J. Meteor. Soc. Japan,* **71,** 685–700.

——, and Coauthors, 2001: Retrieved vertical profiles of latent heating release using TRMM rainfall products for February 1998. *J. Appl. Meteor.,* **40,** 957–982.

Tiedke, M., 1989: A comprehensive mass flux scheme for cumulus parameterization in large-scale models. *Mon. Wea. Rev.,* **117,** 1779–1800.

Viltard, N., C. Kummerow, W. S. Olson, and Y. Hong, 2000: Combined use of the radar and radiometer of TRMM to estimate the influence of drop size distribution on rain retrievals. *J. Appl. Meteor.,* **39,** 2103–2114.

Webster, P. J., 1983: Mechanisms of monsoon low-frequency variability: Surface hydrological effects. *J. Atmos. Sci.,* **40,** 2110–2124.

Wilheit, T. T., and K. D. Hutchison, 2000: Retrieval of cloud base heights from passive microwave and cloud top temperature. *IEEE Trans. Geosci. Remote Sens.,* **38,** 1253–1259.

Yanai, M., S. Esbensen, and J.-H. Chu, 1973: Determination of bulk properties of tropical cloud clusters from large-scale heat and moisture budgets. *J. Atmos. Sci.,* **30,** 611–627.

Yang, S., and E. A. Smith, 1999: Moisture budget analysis of TOGA COARE area using SSM/I-retrieved latent heating and large-scale Q2 estimates. *J. Atmos. Oceanic Technol.,* **16,** 633–655.